

Stardust—An artificial, low-velocity “meteor” fall and recovery: 15 January 2006

D. O. REVELLE^{1*} and W. N. EDWARDS²

¹Atmospheric, Climate and Environmental Dynamics, Earth and Environmental Sciences Division,
Los Alamos National Laboratory, Los Alamos, New Mexico 87544, USA

²Department of Earth Sciences, University of Western Ontario, London, Ontario, N6A 5B7, Canada

*Corresponding author. E-mail: revelle@lanl.gov

(Received 06 April 2006; revision accepted 24 November 2006)

Abstract—On January 15, 2006, Stardust, a man-made space capsule, plummeted to Earth for a soft landing after spending seven years in space. Since the expected initial speed of the body was about 12.9 km/s, a four-element ground-based infrasound array was deployed to Wendover, Nevada, USA, to measure the hypersonic booms from the re-entry. At a distance of ~33 km from the nominal trajectory, we easily recorded the weak acoustic arrivals and their continued rumbling after the main hypersonic boom arrival. In this paper, we report on subsequent analyses of these data, including an assessment of the expected entry characteristics (dynamics, energetics, ablation and panchromatic luminosity, etc.) on the basis of a bolide/meteor/fireball entry model that was specifically adapted for modeling a re-entering man-made object.

Throughout the infrasonic data analyses, we compared our results for Stardust to those previously obtained for Genesis. From the associated entry parameters, we were also able to compute the kinetic energy density conservation properties for the propagating line source blast wave and compared the inviscid theoretical predictions against observed ground-based infrasound amplitude and wave period data as a function of range. Finally, we made a top-down bottom-up assessment of the line source wave normals propagating downward into the complex temperature/sound speed and horizontal wind speed environment during January 15, 2006. This assessment proved to be generally consistent with the signal processing analysis and with the observed time delay between the known Stardust entry and the time of observations of infrasound signals, and so forth.

INTRODUCTION AND OVERVIEW

Large Meteoroid Entry

Large meteoroids, having initial velocities ranging from ~11–73 km/s to be bound to the solar system, can produce strong shock waves upon entry into Earth’s atmosphere while ablating, fragmenting, decelerating, and producing copious amounts of luminosity with heat-transfer flow regimes ranging from the extremes of free-molecular to continuum flow. In this process, we must deal with their generally unknown characteristics of shape, radius, speed, composition, degree of porosity, rotation and tumbling, and so forth. We have previously developed detailed algorithms for evaluating their expected entry characteristics as well as the concomitant production of light, heat, mechanical waves (including the full spectrum of acoustic-gravity waves), ionization, and so forth. With the entry of the Stardust space capsule at 12.9 km/s, we felt that we had a very good surrogate for an

artificial, albeit low-speed, meteor entry that could be extensively studied and compared against our “standard” repertoire of bolide source evaluation techniques.

The Stardust Experiment

We monitored the re-entry of Stardust at the airport in Wendover, Nevada, USA (40.7154°N, –114.0357°W), using a temporary four-element infrasound array (and two co-located seismometers) whose location was along a closest approach ground track of 32.6 km at an altitude of 43.07 km from the nominal pre-flight NASA entry trajectory (see Fig. 2 for details). This pioneering NASA mission, which had been in space for nearly seven years, had an initial mass of ~45.8 kg. The Stardust capsule re-entered after separation from the main spacecraft and plunged into the atmosphere at ~12.9 km/s at an initial entry angle of ~8.2°. NASA had of course also done a pre-flight re-entry analysis of this body that utilized a charring ablation heat shield for protection of

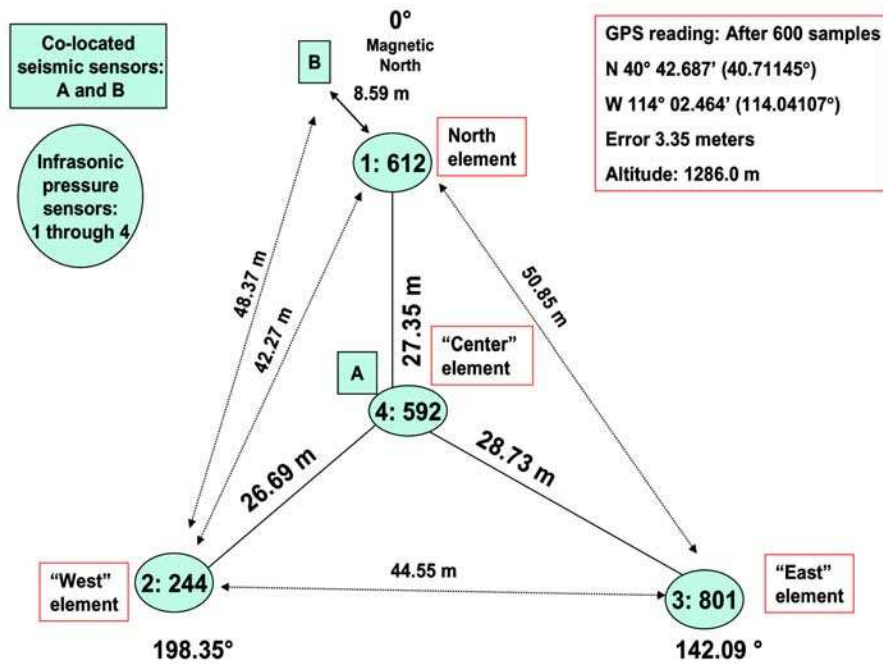


Fig. 1. Wendover infrasound array details.

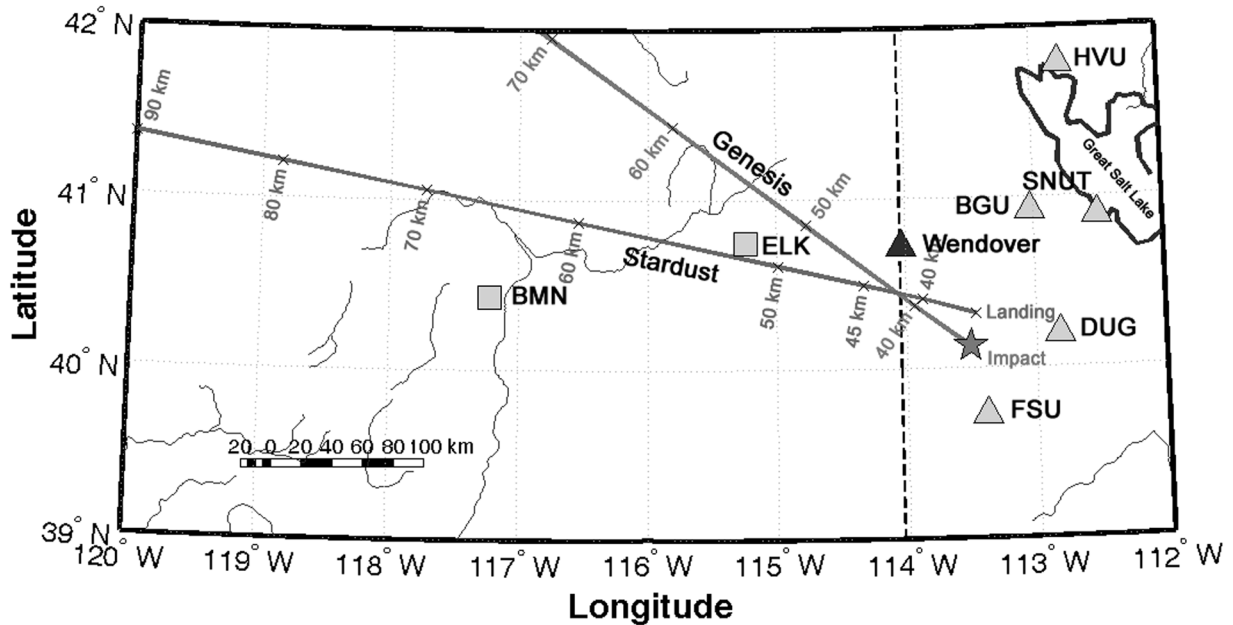


Fig. 2. A geographical overview of Stardust entry.

the spacecraft instruments which in many ways is similar to our subsequent findings below. This is only the second time that this type of heat shield has been used since the Mercury-Gemini-Apollo era, with the other example being the Genesis re-entry that we also monitored infrasonically about 1.5 years earlier at the same location. The Stardust experiment was carrying a valuable cargo of cometary dust particles that had

been collected from comet Wild-2 (D. Brownlee, personal communication). Thus, in addition to the significant results that Dr. Brownlee and his colleagues were anticipating regarding the collection of cometary materials from the onboard payload, we also wanted to demonstrate to both the planetary science and aerospace engineering communities that significant re-entry science could also be performed

using the inferred properties of the re-entry payload itself and its interactions with the Earth’s atmosphere as an artificial meteor, after its infrasound wave signals were recorded and analyzed in detail. This, we believe, we have done, as is subsequently established in this paper.

Table 1b, in addition to providing some of the most important physical properties of the Stardust spacecraft, also lists properties of Hayabusa, the forthcoming Japanese Aerospace Exploration Agency experiment, in some detail. As of this writing (October 2006), it would appear that this spacecraft will try for a return to Earth in 2010 over Australia, hopefully with a cargo of sampled asteroidal material.

PREDICTION OF THE STARDUST ENTRY ENVIRONMENT

Preliminary Remarks

It was challenging to model a real re-entry where many parameters are reasonably well known, as opposed to the usual bolide entry cases that we have evaluated repeatedly in the past. Our standard bolide model (ReVelle et al. 2004; ReVelle 2005) incorporates a number of useful features and physics necessities, including laminar versus turbulent convective heat transfer through the gas cap as well as the full shock wave radiative heating calculated independently of the gas-cap opacity (and not computed strictly in the much more common “diffusion” approximation). It also includes a triggered progressive fragmentation model that results in a cascade of continuous fragmentation events once initiated by the stagnation pressure having exceeded the body’s breaking strength for these large bodies. The latter breakup strength values are also explicitly included within the scheme for all known meteoroid types, but this breakup feature was intentionally turned off during our modeling efforts below. All heating and momentum variations were all physically linked as a function of the various Knudsen number-based flow regimes encountered during entry as well. The model can be run in either a homogeneous or a porous meteoroid mode and is capable of approximating the expected luminous output (Watts/steradian) in a panchromatic passband as well as a total power budget as a function of height or of time.

First, the theoretical modeling option that we are using in order to understand the Stardust entry assumes a homogeneous body that certainly is not generally applicable to this complex capsule. We also have a porous body option in the entry code, but this complex capsule is also clearly not a case of uniform porosity, as was assumed in our prior code development. What is most important for the case of ballistic, nonlifting entry at low entry velocities is first the mass-to-area ratio (proportional to the modified ballistic entry parameter), and second, the body radius and its associated shape and/or its changes during entry. Since Stardust is approximately hemispherical, we will assume that a hemisphere adequately

captures the shape of the body for simplicity. This corresponds to the standard shape factor of meteor physics, namely, $S_f = A/V_0^{2/3}$ = frontal cross-sectional area, A divided by the meteor volume, V_0 , taken to the 2/3 power $\cong 1.9192$ compared to the standard value $\cong 1.209$ for a sphere, for example. Since we knew the total initial capsule mass (=45.8 kg) for Stardust (and 225.0 kg for Genesis), and assuming an initial hemispherical shape, we immediately calculated the equivalent bulk density for a body that was assumed to be of uniform density. In this way, we determined bulk densities of 327.97 kg/m³ for Stardust and 244.73 kg/m³ for Genesis, respectively.

To begin our entry modeling, we began simulations with a bulk density of 1500.0 kg/m³, which corresponds to an approximate upper limit density for ceramic-type materials with no voids, and successively decreased this value by a factor of 2 until a reasonable convergence had been reached between theory and observations for modeling of the instantaneous velocity for both of these man-made capsules (in order to including possible measurement errors, etc.). Initial radius values determined in this way for Genesis ranged from ~0.415 to 0.659 m over the bulk density range from 1500.0 to 375 kg/m³, while the same procedure for Stardust resulted in initial radius values ranging from ~0.244 to 0.388 m, respectively. The corresponding computed hemispherical mass/area ratios for these cases ranged from 415.28 to 164.80 kg/m² for Genesis and from 244.29 to 96.95 kg/m² for Stardust. (This iterative reduction in the assumed bulk density caused a corresponding increase in the body radius and a predicted increase in the luminosity of the body during entry with all else the same).

In addition, in an attempt to capture the expected shape changes on the heat shield during entry, we have now assigned μ , the shape change parameter, the value 0.10 during the computations, which has been found to be numerically almost indistinguishable from the $\mu = 0$ limit for these sets of conditions. This represents a severe case of blunting, as was to be expected for this high an entry speed. The observed velocity profiles for both Genesis and Stardust were provided courtesy of Dr. P. Desai at the NASA Langley Research Center, Hampton, Virginia, USA, where the measurements are shown in comparison with our series of entry modeling velocity solutions for both spacecraft. These new results are presented in Figs. 3a and 3b for Genesis and Stardust, respectively.

The entry dynamics solutions that have been presented in this paper are all for a stagnation point, laminar gas-cap boundary layer, i.e., for a stably oriented nonturbulent gas cap flow field in direct contrast to the results that we provided previously for Genesis (ReVelle et al. 2005). Those earlier Genesis results resulted from the formal prediction of a turbulent gas-cap boundary layer during entry. This was possible for a dynamically unstable tumbling body (which we further approximated as a sphere) that was predicted to develop during entry and was based on a Reynolds number

Table 1a. Stardust: Inputs for entry dynamical and panchromatic luminosity calculations and wave normal path evaluations.

Initial mass (kg)	45.8
Initial radius (m). Hemispherical shape initially: oriented, nonturbulent gas-cap, boundary layer flow	0.2443 m ($\rho_m = 1500 \text{ kg/m}^3$) to 0.3878 m ($\rho_m = 375 \text{ kg/m}^3$) ^a
Initial velocity (km/s)	12.90
Zenith angle of radiant (°)	81.8
Vector heading azimuth (°)	90.50° at 41.13 km (available from Dugway radar data)
Shape factor: hemisphere	1.919158
Shape change factor μ	0.10
Kinetic energy depletion factor D (99% KE depletion)	4.605
Homogeneous or porous model	Homogeneous
Uniform bulk density of the Stardust capsule	$1.5 \cdot 10^3 \text{ kg/m}^3$, $7.5 \cdot 10^2 \text{ kg/m}^3$, $3.75 \cdot 10^2 \text{ kg/m}^3$
Ablation parameter, σ changes	Variable $\sigma(z)$
Atmosphere model type	Nonisothermal, hydrostatic atmosphere
Season of the year	Winter atmospheric model

^aNominal bulk density value, closest to fitting the observed NASA velocity flight data.

Table 1b. Genesis in comparison to other forthcoming entry vehicles.

	Genesis	Stardust	Hayabusa
Date	2004 September 08	2006 January 15	2010 ?
Time, local	9:54 A.M. MDT	3:00 A.M. MDT	3:00 A.M.
Mass (kg)	225	45.8	18
Diameter \varnothing (m)	1.52	0.811	0.40
Entry speed at 135 km (km/s)	11.0	12.9	12.2
Entry angle (°)	8.0	8.2	12.0
Spin rate (rpm)	15	15	2
Aerodynamic stability	Not stable	Not stable	Stable
Peak heat rate (W/cm ²)	750	1200	~1500
Peak deceleration (Earth g)	28	34	45
Peak brightness (from 100 km)	–	–	–
Landing site	UTTR, Utah	UTTR, Utah	Australia
Heat-shield material	Carbon-carbon	Phenol impregnated carbon ablator (PICA)	Carbon phenolic ablator
Thickness	1.5 inches over insulator	2 inches	–
Sample returned	Solar wind	Comet dust, ISD	Asteroid dust

turbulent boundary layer transition criterion that had been developed previously for dynamically unstable and tumbling meteor-fireballs (ReVelle 1979). We based our assumptions for these earlier spherical turbulent boundary layer results on comments made in a NASA briefing at the Jet Propulsion Laboratory by Burnett in March 2004; these are summarized in Table 1b. Our newest results, computed for purely oriented flow *without* random tumbling and dynamical instability, i.e., for a stable-oriented type flow, are presented in the current paper for both Genesis and Stardust (*assuming* that a turbulent boundary layer gas cap region did not exist during entry). It should also be pointed out that we have used a generalized meteor ablation model and not the frontal heat shield solution for a charring ablator typical of the Apollo re-entry programs and that were readily available for protection of the Genesis and Stardust capsules during entry. Nevertheless, the current level of agreement between theory and measurements appears acceptable (Jenniskens et al. 2005, 2006).

Finally, our entry inputs also correspond to a case of constant entry angle, θ ($=8.2^\circ$), which is not exactly the case.

We proceed, however, with a constant entry angle solution (equal to the initial value at the interface entry altitude where the body force component/mass along the trajectory just balances the acceleration due to gravity). This was predicted to occur at ~ 93.8 km for Stardust (and at ~ 91.4 km for Genesis). However, it is not expected for this angle to significantly change until much lower altitudes. This very small horizontal entry angle (as was also the case for Genesis) is very near to the validity limit for the steep angle solution for ballistic, nonlifting re-entry evaluated in Cartesian coordinates.

With all of these values supplied to the entry code, we proceeded as described above. In this work, we have adapted an entry model (ReVelle 2001, 2002, 2005) that was originally developed for modeling the ballistic entry of meteor-fireballs (bolides). Table 1a lists inputs we have used to model the Stardust re-entry with some of the details taken from Burnett (2004).

Below ~ 30 km for the NASA nominal planned re-entry, the entry angle would be expected to quickly become nearly

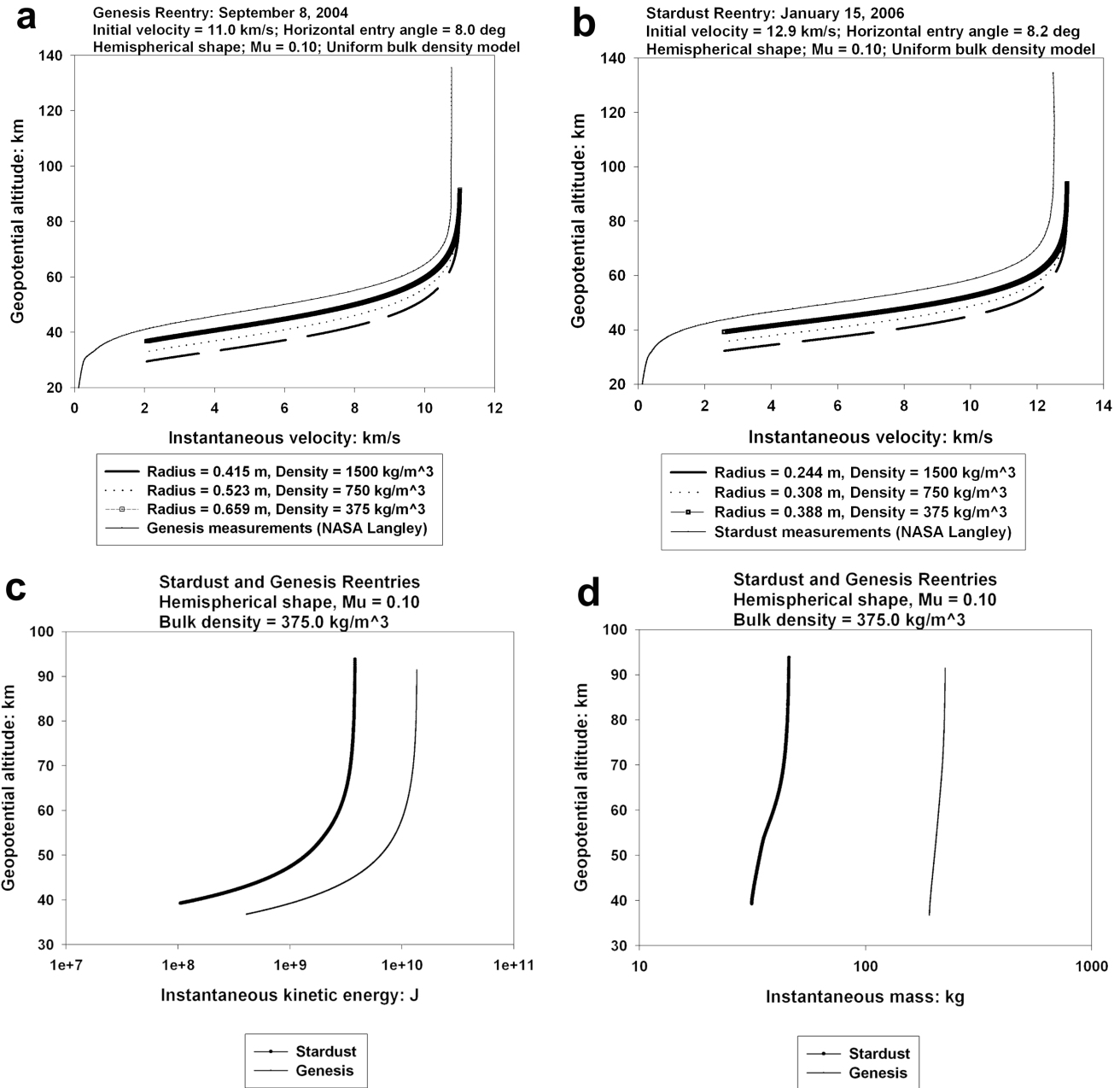


Fig. 3. a) Genesis entry environment predictions: velocity. b) Stardust entry environment predictions: velocity. c) Stardust and Genesis environmental predictions: kinetic energy. d) Stardust and Genesis entry environment predictions: mass loss.

vertical, so that $Z_R = 0^\circ$, because of the effects of the acceleration due to gravity and in the absence of significant horizontal atmospheric winds.

Velocity, Kinetic Energy, Mass Loss, and the Ablation Parameter σ

In Fig. 3a, we have plotted the measured Genesis velocity profile (P. Desai, personal communication) and our corresponding theoretical solutions. In Fig. 3b, we have also plotted the measured Stardust velocity profile (P. Desai,

personal communication) and our corresponding theoretical solutions. In both re-entry cases, there is a definite convergence of the theoretical solutions to the measured values as the bulk density of the initially hemispherical body is decreased in successive steps to values approaching 375 kg/m³ or perhaps slightly lower. Radii for Genesis computed in this way range from 0.415 to 0.659 m, in comparison to the radius of the actual body of 0.76 m. Radii for Stardust computed in this way range from 0.244 to 0.388 m, in comparison to the radius of the actual body of 0.405 m. Thus, at the lowest bulk densities assigned above,

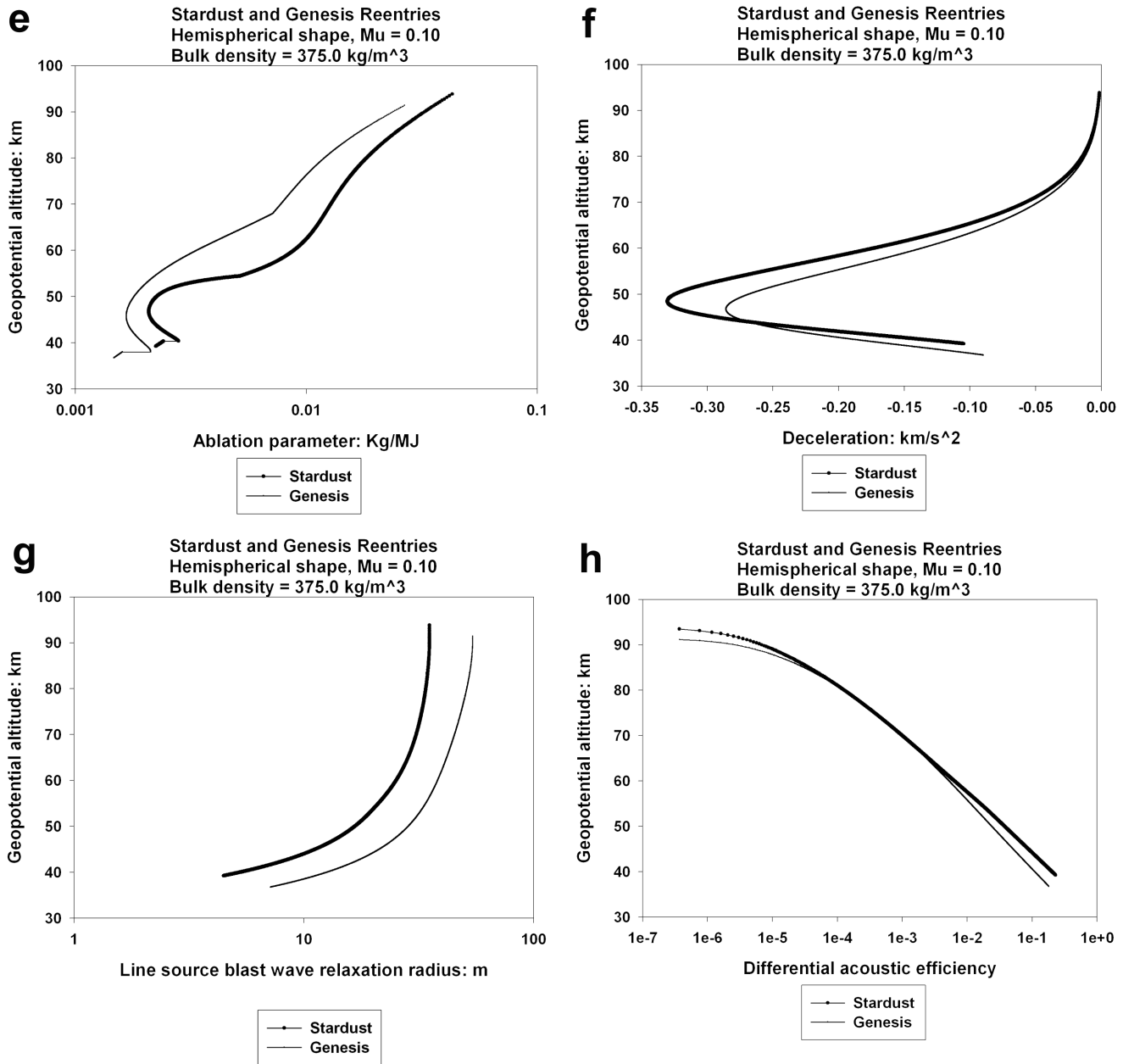


Fig. 3. *Continued.* e) Stardust and Genesis entry environment predictions: ablation parameter σ . f) Stardust and Genesis entry environment predictions: deceleration. g) Stardust and Genesis entry environment predictions: line source blast radius. h) Stardust and Genesis entry environment predictions: differential acoustic efficiency.

we are recovering the original radius of the body, assuming, however, that it is homogeneous in its density throughout, which is clearly not the case.

In Figs. 3c–e, we have plotted the kinetic energy, mass loss (where we have predicted a mass loss of ~31.5% for Stardust while the corresponding earlier prediction for Genesis was ~14.8%, if these were both real bolides), and the expected corresponding ablation parameter for the Stardust entry, respectively. The Stardust ablation loss, although unreasonably high, resulted from the smaller size and higher

entry velocity in comparison to Genesis. Nonetheless, the computed end height for the two entries was nearly compensated by the change in physical parameters of the two bodies and their entry speed. For Genesis, we computed an end height of 36.76 km at a speed of 2.06 km/s, while for Stardust we computed a corresponding end height of 39.23 km at a speed of 2.58 km/s. As expected, all parameters are quite reasonable in magnitude, given the rather low entry velocities. Computer calculations that were done with the turbulent boundary layer (gas-cap) transition removed agreed much

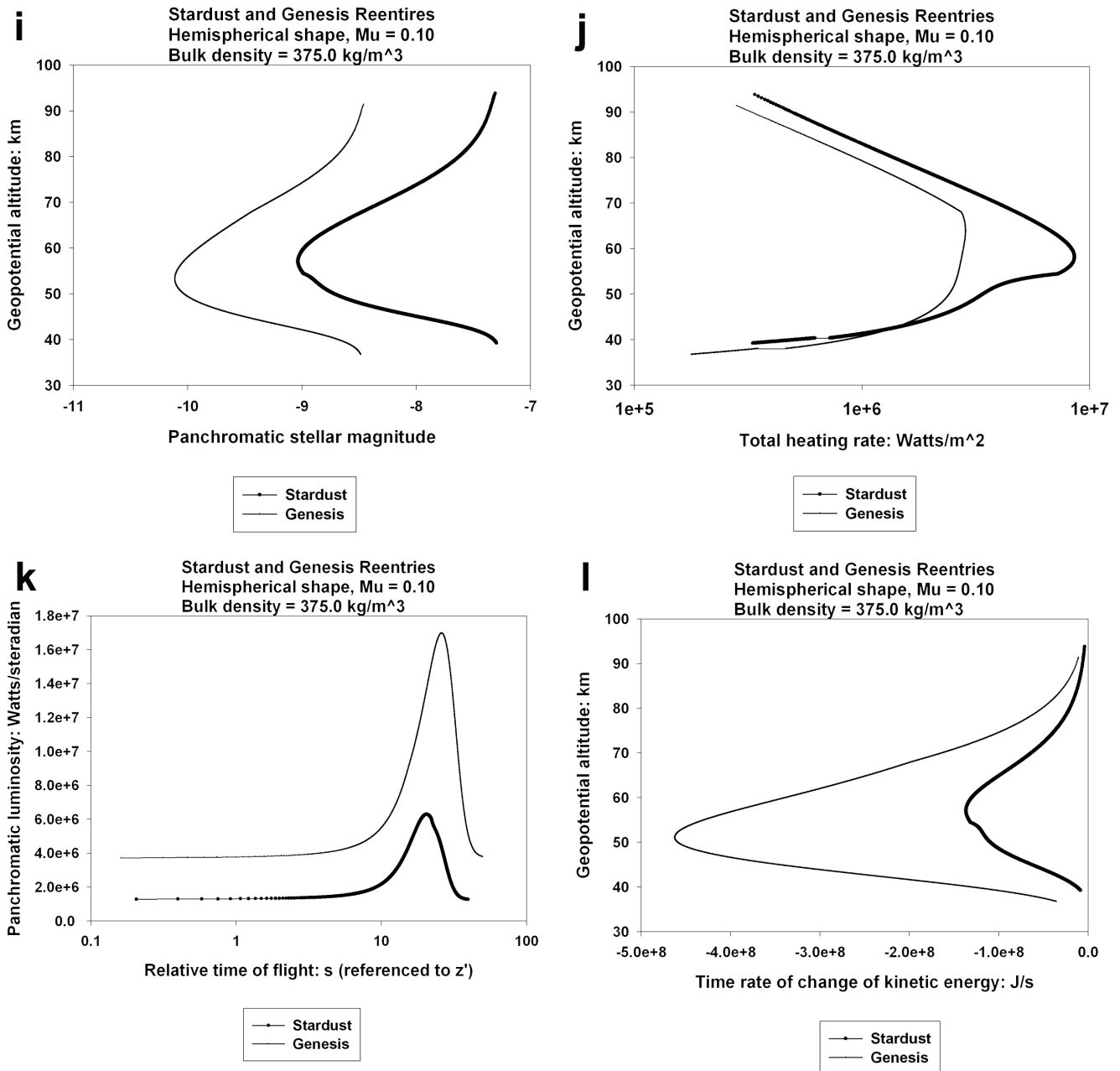


Fig. 3. *Continued.* i) Stardust and Genesis entry environment predictions: panchromatic luminosity (at 100 km in the zenith). j) Stardust and Genesis entry environmental predictions: total heating rate. k) Stardust and Genesis entry environmental predictions: the power time curve. l) Stardust and Genesis entry environmental predictions: time rate of change of the kinetic energy.

better with the official NASA velocity measurements for both the Stardust as well as the Genesis re-entry velocity behavior.

Deceleration, Line Source Blast Wave Radius, and the Differential Acoustic Efficiency

In Figs. 3f–h, we have plotted the deceleration, line source blast wave relaxation radius, and differential acoustic efficiency parameters. Reasonable agreement in both geopotential height and in terms of the number of g 's

experienced during entry was once again found between our deceleration predictions and those officially made by NASA (Burnett 2004). Blast wave radii for an assumed nonbreaking body were found in the range from ~ 10 – 40 m depending explicitly on height. Throughout this work, we have used the line source explosion blast wave radius formulation, $R_0 \cong M \cdot d$ as utilized in our bolide computations for defining the nonlinear “explosion zone” surrounding the cylindrical line source trajectory. The lack of complete applicability of this spatial scale to the very low-speed supersonic flow

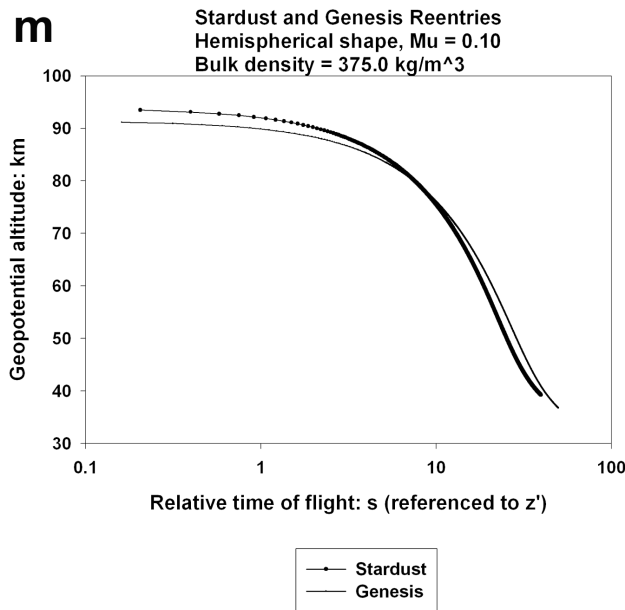


Fig. 3. *Continued.* m) Entry environmental predictions: height versus time relationship.

regime will be discussed briefly later. This scale also has consequences for the very large differential acoustic efficiency determined at low heights as will also be subsequently discussed below.

Panchromatic Luminosity, the Power-Time Curve, and the Total Heating Rate

In Figs. 3i–k, we have plotted the panchromatic luminosity (expressed in stellar magnitude as observed at an altitude of 100 km in the zenith), the power-time curve (expressed in Watts/steradian), and the total heating rate (expressed in Watts/m²). Our peak total heating rate for Stardust was $\sim 8.58 \cdot 10^6$ Watts/m² and $\sim 2.85 \cdot 10^6$ Watts/m² for Genesis, respectively.

Optical video recordings of the Stardust entry was made in Nevada by A. Hildebrand and colleagues and by the UWO group (Department of Physics, University of Western Ontario, Canada) in Wendover. A detailed comparison between our theoretical optical predictions and these data will be made in a later paper, but preliminary calibrations of the UWO video have a peak maximum optical magnitude of -8 ± 2 and our maximum panchromatic magnitude prediction is $\cong -9$.

Finally, in Figs. 3l–m, we have plotted the time rate of change of the kinetic energy and of geopotential height versus time of flight for Stardust and Genesis, respectively.

Total Power Budget

Following ReVelle et al. (2004), we have also plotted all of the differential efficiencies predicted for the Stardust and

Genesis entries. These results are plotted in Figs. 4a and 4b for Stardust and Genesis, respectively. The only unusual values are the differential acoustic efficiencies below ~ 45 km, which exceed about 10%. As a direct result, of course, the corresponding total power budget is close to exceeding 100% below this altitude as well. Later on we will show that these large values are due physically to the fact that we had used the hypersonic line source blast wave analog theory throughout to make pressure wave amplitude predictions. For Mach numbers ≤ 5 (where dissociation of the neutral gas begins for progressively increasing speeds), we have constructed a transitional approach to a fully supersonic flow theory result that we will utilize later and that predicted significantly smaller differential acoustic efficiency values. In all other ways, our results show that we have accounted for a very large percentage of all of the power lost during atmospheric entry for both Stardust and Genesis. The only exception to this statement is at the very earliest time of entry when presumably more thermal power in the form of heat was generated than we have presently predicted.

MEASUREMENTS AND DETECTION ANALYSES FOR THE STARDUST RE-ENTRY

Deployment of Infrasound Array: Wendover, Nevada

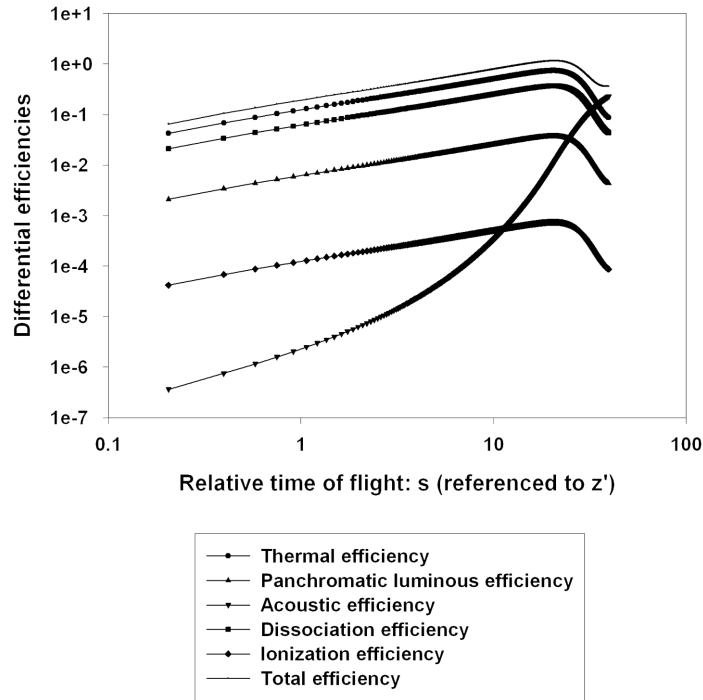
All of our detection equipment was driven in a government van from Los Alamos, New Mexico, to Wendover, Nevada, with just enough time to set up the array and check out the equipment for about 24 hours prior to the re-entry event. We deployed the following primary set of field equipment at Wendover to monitor the infrasonic waves:

1. Four Chaparral (previously Globe Universal Sciences) low-frequency capacitance differential microphones: Response: 3 dB down nominally at 0.02 and 300 Hz
2. A Teledyne-Geotech 24 bit digitizer and GPS timing unit
3. Porous, 16 m long soaker hoses—six sets at equal angular spacing at each microphone

The digital sampling rate we employed was 100 Hz, so that we have an imposed sampling cut-off frequency in all of our fast Fourier transform (FFT) calculations corresponding to frequencies below the concomitant Nyquist value, i.e., 50 Hz. The deployment arrangement at the Wendover, Nevada, airport is indicated in Fig. 1. The location of the array was some 33 km to the northeast of the expected entry flight path. At the expected time of re-entry, we were located to the north end of the airport near our optical all-sky camera system, which also monitored the Stardust re-entry. All three people heard one muffled hypersonic boom from this event. It was also witnessed visually at our location and was quite spectacular.

Recordings of the infrasound from the Stardust re-entry were obtained with a ground-based acoustic array similar to

a Stardust Reentry: Total power balance and differential efficiencies-
 Uncorrected for supersonic flow at low heights; Hemispherical shape
 $\mu = 0.10$; Initial velocity = 12.9 km/s; Horizontal entry angle = 8.2 deg
 Bulk density = 375.0 kg/m³, Initial radius = 0.3878 m; Winter model atmosphere



b Genesis Reentry: Total power balance and differential efficiencies-
 Uncorrected for supersonic flow at low heights; Hemispherical shape
 $\mu = 0.10$; Initial velocity = 11.0 km/s; Horizontal entry angle = 8 deg
 Bulk density = 375.0 kg/m³, Initial radius = 0.6592 m; Summer model atmosphere

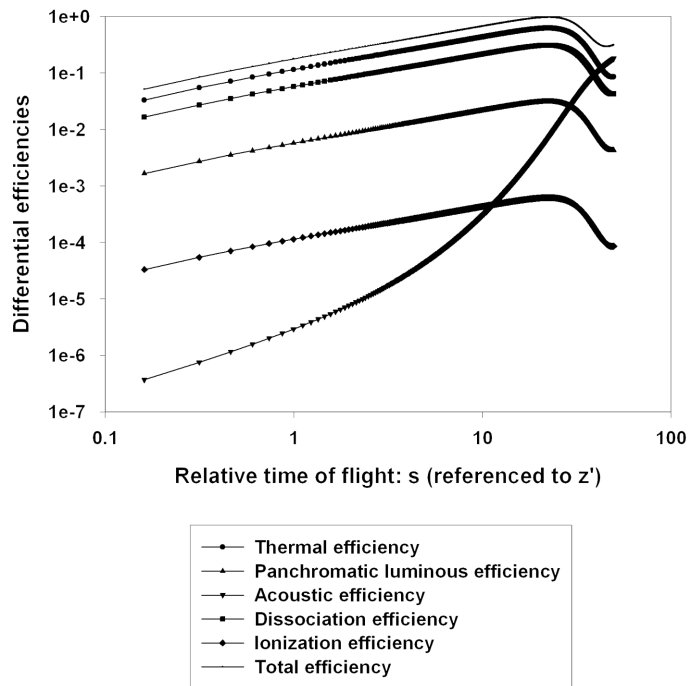


Fig. 4. a) Stardust: hypersonic aerodynamic total power balance and differential efficiencies, uncorrected for supersonic flow effects at low heights. b) Genesis: hypersonic aerodynamic total power balance and differential efficiencies, uncorrected for supersonic flow effects at low heights.

the single microphone measurements made on each ship that were placed directly beneath the planned ground track during the Apollo reentries of the 1970s (Hilton et al. 1972; Henderson and Hilton 1974a, 1974b). In those earlier re-entry detections, three ships usually participated in the measurements during either ascent or re-entry (or both) so that array capabilities were available if needed. In these earlier measurements, the multiple microphones were very closely spaced and were also carefully placed on individual ships so that for the high Mach number and nearly vertical arrivals, multiple reflections off the ship superstructures could be minimized (Hilton and Henderson 1972). Re-entry speeds were similar to that of Stardust and horizontal flight paths angles varied considerably from steep to shallow for these earlier entry tests.

Co-located seismic detections were also made simultaneously at two seismometers during the Stardust re-entry measurement campaign; these are so important that they will be analyzed in detail in a separate companion paper (Edwards et al., Forthcoming). Details of the locations of the microphones and seismometers are indicated in Fig. 1, and the geographic layout of the region, including nearby seismic stations, is indicated in Fig. 2.

Signal Detection and Analyses

In our data-processing work, we have used the standard signal-processing detection and location software, Matseis/Infratool (available as public domain software from Sandia National Laboratory in Albuquerque, New Mexico) to analyze data from our temporary four-element infrasound array at the airport in Wendover, Nevada. An unfiltered channel plot of the pressure wave amplitude versus time of the initial N wave hypersonic boom arrival is given in Fig. 5a. A similar unfiltered channel plot for the second set of signal arrivals (delayed by ~ 10 s from the initial arrivals) is plotted in Fig. 5b. Tabular values characterizing both the amplitude as well as the dominant wave period of these sets of signals is given in Tables 2, 3a, and 3b, respectively. Similar delayed arrivals continue to arrive long after the initial hypersonic boom N wave type “pulse” and as many as five or six additional discrete, albeit lower amplitude and higher frequency arrivals from the proper direction and height (through the arrival trace velocity), can similarly be identified. Although we have not investigated all of these very small amplitude signals in a systematic manner (except for the first delayed set of arrivals shown in Fig. 5b), we note the arrival time of the first of these discrete events.

1. Arrival of the main hypersonic boom signals: 10:01:04.2 UTC
2. First delayed signal set arrived at 10:01:13.5 UTC

A digital FFT power spectral density (PSD) plot of the signal power is given in Figs. 6a and 6b (for the initial set of hypersonic boom arrivals for frequencies < 50 Hz and for the

second set of delayed arrival for the same frequency range). Similar to other well-known PSDs of N waves, a multiple-lobed peaked FFT on the high-frequency side of the main acoustic peak is also clearly evident (Garrick and Maglieri 1968).

Clearly the peak acoustic energy is found to be at a dominant frequency in this case of about 5–6 Hz (Fig. 6a), with slightly higher frequencies found in Fig. 6b (in good agreement with our zero-crossing measurement technique indicated in Tables 2, 3a, and 3b.) The spurious sharp peak at lower frequencies of ~ 1.5 –2 Hz is due to interference from the prevailing Microbaroms and also due to signal aliasing effects because of the small number of samples at lower frequencies compared to those available at the peak acoustic frequency set by the data sampling window length. In addition, a spectrogram of power levels versus frequency as a function of time is also indicated in Fig. 7. In this latter figure, it is clearly seen that, in addition to the main hypersonic boom arrivals and the subsequent rumbling for about 2 minutes after the main events arrived, a clear set of signals from an extremely slow-moving point source whose heading was generally from west to east at this very early hour of the morning, is also clearly evident. This is simply a set of signals from a locomotive passing through Wendover at the time as was noted in our separate data log for the Stardust observing campaign.

The main hypersonic boom arrival occurred at approximately 10:01:04.2 UTC, which can be compared with the predicted NASA nominal peak heating entry time that was targeted to have occurred at 09:57:33.42 UTC at 61.5 km as well as the predicted time of drogue deployment at 09:58:55.22 UTC at 32.09 km (P. Desai, personal communication). These times are 51.2 and 133.0 s after the predicted entry interface condition, respectively. From our entry simulations for Stardust, this point of maximum heating should have occurred at an altitude of 57.1 km, which from Fig. 2 would locate this region substantially off to the west from the point of closest approach to the Wendover airport for the Stardust entry trajectory. The 3.513 minute propagation time delay (210.78 s) corresponds to a total slant range distance from the entry trajectory of about 71.67 km, which is roughly comparable to values used below in our wave kinetic energy density conservation numerical approach (assuming a lower atmospheric sound speed of about 0.3453 km/s based on a near-surface temperature of 296.65 K). This estimate puts a reasonable bound on our wave kinetic energy density conservation solution for the independent determination of the source altitude from the infrasonic signal arrivals on the basis of wave energetics conservation alone.

On the basis of the observed signal trace velocity ($\cong 0.535$ km/s corresponding to an elevation arrival angle of $50.54^\circ = \cos^{-1} [c_s/V_{\text{trace}}]$) coincident with the main hypersonic boom arrival at a horizontal range of 32.6 km from a source height of 42.7 km (the nominal position of the

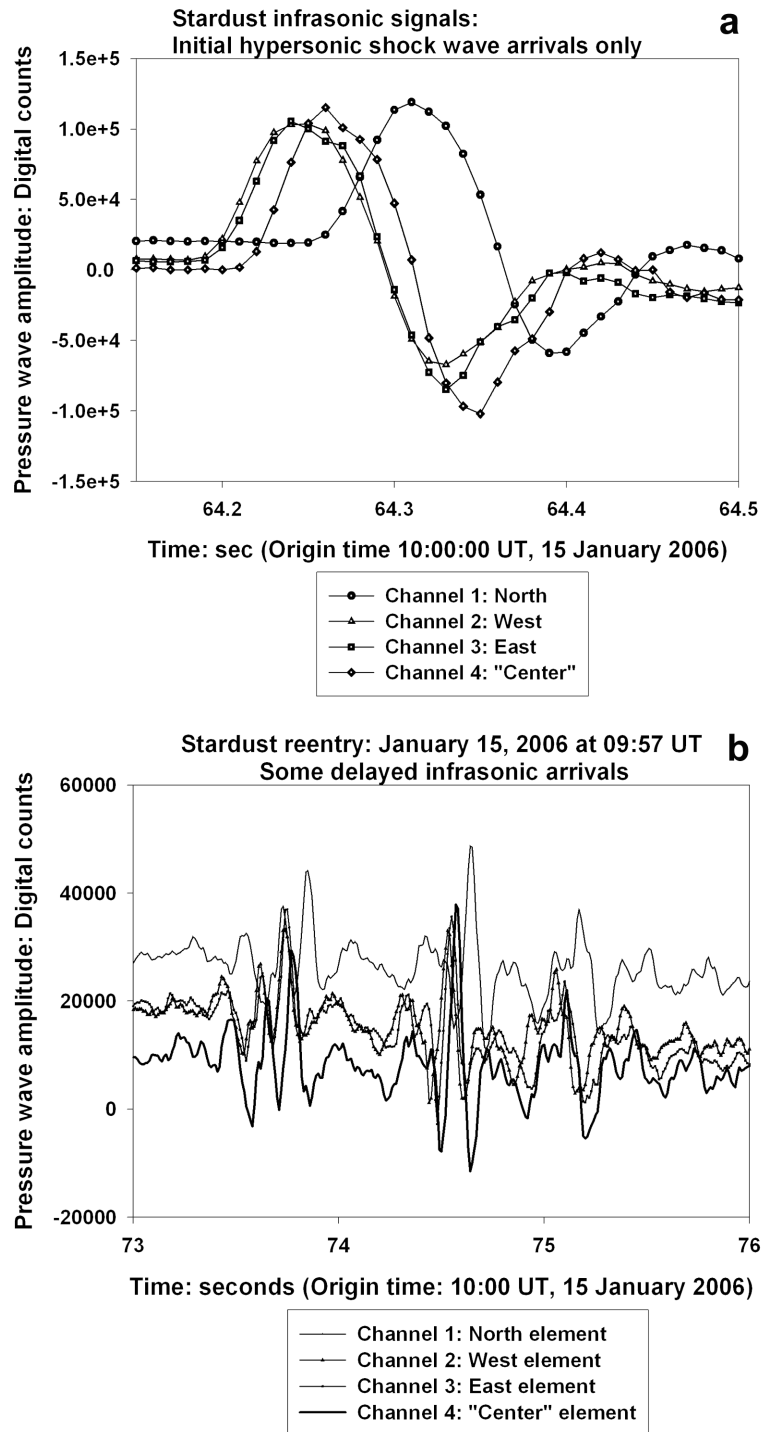


Fig. 5. a) Initial N wave arrivals (unfiltered). b) Second set of wave arrivals (unfiltered).

Stardust entry trajectory from the Wendover airport), we can deduce a source height from 39.6 km for a straight line ray path (unrefracted at this point by assumption—see Figs. 8a–d with the corresponding vertical atmospheric structure parameters, i.e., the temperature and the horizontal wind data plotted in Figs. 9a–c) traveling downward from this

rapidly moving point source. This is only about 7.8% lower than the NASA-predicted height for this position of closest approach to the Wendover airport. This corresponds to values at the perpendicular point along the trajectory. In the above expression, c_s is the adiabatic thermodynamic sound speed and V_{trace} is the horizontal trace velocity (the apparent speed

Table 2. Stardust: Measured infrasound signal properties for both the first and the second set of infrasonic arrivals.^a

Maximum amplitude (Pa)	1.153 ± 0.096 (0.207 ± 0.038) ^b
Peak-to-peak amplitude (Pa)	1.798 ± 0.191
Prior noise (RMS amplitude)	$7.90 \cdot 10^{-3} \pm 4.7 \cdot 10^{-3}$
Post noise (RMS amplitude)	$9.20 \cdot 10^{-3} \pm 5.30 \cdot 10^{-3}$
Integrated signal energy	
N wave signal	$7.550 \pm 1.154 \text{ Pa}^2$
Prior background noise	0.0348 Pa^2
Post background noise	0.3530 Pa^2
Mean background noise	$0.1939 \pm 0.0272 \text{ Pa}^2$
Standard deviation of mean noise between prior and post energy	$2.2505 \cdot 10^{-1} \text{ Pa}^2$
Total signal energy (bolide – mean background)	$7.356 \pm 1.154 \text{ Pa}^2$
Main signal/noise (peak-to-peak)	SNR: 226.1 ± 136.2
Dominant signal frequency	5.00 (z.c.) $\pm 0.2506 \text{ Hz}^c$
Corresponding dominant period	0.200 (z.c.) $\pm 0.01 \text{ s}^c$
Dominant period: second arrival ^b	0.162 (z.c.) $\pm 0.014 \text{ s}^b$

^aAfter converting raw amplitudes in digital counts using 1) $3.77 \cdot 10^{-6}$ volt/count, 2) 0.04 volt/microbar or 400 mV/Pa; 1 microbar = 0.10 Pa, and 3) band-pass utilized: 0.50–24.5 Hz (see next footnote).

^bMeasured signal properties for the second set of arrivals (delayed by ~10 s from the initial N wave arrivals).

^cIn order to determine the mean wave period, the standard zero-crossing (z.c.) technique was used by taking the time difference between the first two zero crossings and doubling that value to realistically account for the negative N wave phase as well as the positive phase value. Standard FFT techniques for this case produced a wave period of 0.20 s.

Table 3a. Stardust numerical solutions: Kinetic energy density conservation approach ($1 \text{ kt} = 4.185 \cdot 10^{12} \text{ J}$); search interval = 1.0 km; surface air density = 1.225 kg/m^3 . Infrasonic evaluations: Nominal differential acoustic efficiency (hypersonic values).

Type of approach	Main infrasonic arrival
$R_{\text{obs}} = 32.6 \text{ km}$ (horizontal range) for $z = 42.7 \text{ km}$: NASA entry nominal, closest horizontal range and source height	$\tau = 0.200 \text{ s}$, $\Delta p = 1.153 \text{ Pa}$
$E_{\text{so}}^a = 3.8108 \cdot 10^9 \text{ J}$ $= 9.1058 \cdot 10^{-4} \text{ kt}$	$y = 1/2$: linearized, geometrical acoustics ray propagation regime $d' = 170.30 \text{ km}$ (85.15 km) ^b
Method a ^c : E_s	$= 2.437 \cdot 10^{-5} \text{ kt}$
Method b ^d : E_s^e	$= 1.557 \cdot 10^{-6} \text{ kt}$
Method c ^f : E_s^e	$= 3.176 \cdot 10^{-6} \text{ kt}$ ($1.383 \cdot 10^{-5} \text{ kt}$) ^b
Method d ^g : source height (km)	$z = 48.08 \text{ km}$ (37.39 km) ^b
Method e ^h	Multiple solutions: $z \cong 35\text{--}38 \text{ km}$ ($37.5\text{--}41 \text{ km}$) ^b and for $z \cong 77\text{--}93 \text{ km}$ ($67.5\text{--}79 \text{ km}$) for $R_0 = 5\text{--}25 \text{ m}^i$

^aInitial atmospheric kinetic energy for a 45.8 kg mass moving at 12.9 km/s.

^bNominal case except for doubled surface wave amplitude.

^cUSAF Technical Applications Center, Patrick Air Force Base, Florida, USA (observed wave period only).

^dLine source (observed wave period and range only).

^eUnlike previous treatments in ReVelle et al. (2004) where these two values were identical at a specified fixed horizontal range, we have now allowed the velocity to vary as predicted theoretically (using the linear least squares, curve-fitted velocity).

^fLine source (observed wave amplitude and range only) at the predicted source height listed in method d.

^gLine source (observed period, amplitude, and range): isothermal atmosphere.

^hIterative line source blast wave radius (kinetic energy density conservation): $R_0 = 10\text{--}30 \text{ m}$, nominal acoustic efficiency (hypersonic flow modeling).

ⁱAlthough consistent energetically, this height regime is inconsistent with our acoustic time delay solutions, as noted earlier.

with which the wave fronts cross the infrasound array horizontally). From these values, we can deduce a total travel distance of 51.29 km, which for a mean typical lower atmosphere sound speed of 0.3314 km/s (corresponding to an air temperature of 273 K) yields a propagation time delay of 154.76 s ($\cong 2.579 \text{ min}$), a value that is somewhat lower than the “observed” travel time of 3.513 minutes. Of course, a substantial part of the temporal discrepancy is that the actual reference time for the point of closest approach to Wendover

is actually later than the peak heating time, but actually before the time of drogue deployment, used above to deduce our time estimate.

We can also anticipate our results below and determine the predicted travel time for a wave normal (equivalent to an acoustic ray in a quiescent stratified medium) corresponding to such heights and total range from the Stardust entry trajectory propagating downward from above to the Wendover airport. We have determined below that the answer

Table 3b. Stardust numerical solutions for the second set of acoustic arrivals (delayed by ~ 10 s): Kinetic energy density conservation approach (1 kt = $4.185 \cdot 10^{12}$ J); search interval = 1.0 km; surface air density = 1.225 kg/m^3 . Infrasound evaluations: Nominal differential acoustic efficiency (hypersonic values).

Type of approach	Main infrasonic arrival
$R_{\text{obs}} = 32.6 \text{ km}$ (horizontal range) for $z = 42.7 \text{ km}$: NASA entry nominal, closest horizontal range and source height	$\tau = 0.162 \text{ s}$, $\Delta p = 0.207 \text{ Pa}$
$E_{\text{so}}^{\text{a}} = 3.8108 \cdot 10^9 \text{ J}$ $= 9.1058 \cdot 10^{-4} \text{ kt}$	$y = 1/2$: linearized, geometrical acoustics ray propagation regime $d' = 768.35 \text{ km}$
Method a ^b , E_{s}	$= 1.206 \cdot 10^{-5} \text{ kt}$
Method b ^c , E_{s}^{d}	$= 6.703 \cdot 10^{-7} \text{ kt}$
Method c ^e , E_{s}^{d}	$= 6.275 \cdot 10^{-7} \text{ kt}$
Method d ^f , source height (km)	$z = 70.486 \text{ km}^{\text{g}}$
Method e ^h	Single possible (inexact) solution: from $z \cong 29.5\text{--}32.5 \text{ km}$ for $R_{\text{o}} = 5\text{--}25 \text{ m}$

^aInitial atmospheric kinetic energy for a 45.8 kg mass moving at 12.9 km/s.

^bUSAF Technical Applications Center, Patrick Air Force Base, Florida, USA (observed wave period only).

^cLine source (observed wave period and range only).

^dUnlike previous treatments in ReVelle et. al. (2004) where these two values were identical at a specified fixed horizontal range, we have now allowed the velocity to vary as predicted theoretically (using the linear least squares, curve-fitted velocity).

^eLine source (observed wave amplitude and range only) at the predicted source height listed in method d.

^fLine source (observed period, amplitude, and range): isothermal atmosphere.

^gAlthough consistent with the line source period, amplitude and range relationship for weakly nonlinear waves, this height regime is inconsistent with our acoustic time delay solutions, as noted earlier.

^hIterative line source blast wave radius (kinetic energy density conservation): $R_{\text{o}} = 10\text{--}30 \text{ m}$, nominal acoustic efficiency (hypersonic flow modeling).

Table 3c. Genesis numerical solutions (revised): Kinetic energy density conservation approach (1 kt = $4.185 \cdot 10^{12}$ J); search interval = 1.0 km; surface air density = 1.225 kg/m^3 . Infrasound evaluations: Nominal differential acoustic efficiency (hypersonic values).

Type of approach	Main infrasonic arrival
$R_{\text{obs}} = 26.1 \text{ km}$ (horizontal range) for $z = 43.07 \text{ km}$: NASA entry nominal, closest horizontal range and source height	Wave period: $\tau = 0.4452 \text{ s}$ (FFT) Wave amplitude: $\Delta p = 3.9995 \text{ Pa}$
$E_{\text{so}}^{\text{a}} = 1.3613 \cdot 10^{10} \text{ J}$ $= 3.2527 \cdot 10^3 \text{ kt}$	$y = 1/2$: linearized, geometrical acoustics ray propagation regime $d' = 112.42 \text{ km}$
Method a ^b , E_{s}	$= 3.529 \cdot 10^{-4} \text{ kt}$
Method b ^c : E_{s}^{d}	$= 4.549 \cdot 10^{-5} \text{ kt}$
Method c ^e : E_{s}^{e}	$= 1.0781 \cdot 10^{-4} \text{ kt}$
Method d ^f , source height (km)	$z = 48.15 \text{ km}$
Method e ^g	Multiple solutions: $z \cong 38\text{--}39 \text{ km}$ and for $z \cong 64\text{--}69 \text{ km}^{\text{h}}$ for $R_{\text{o}} = 20\text{--}40 \text{ m}$

^aInitial atmospheric kinetic energy for a 225.0 kg mass moving at 11.0 km/s.

^bUSAF Technical Applications Center, Patrick Air Force Base, Florida, USA (observed wave period only).

^cLine source (observed wave period and range only).

^dUnlike previous treatments in ReVelle et. al. (2004) where these two values were identical at a specified fixed horizontal range, we have now allowed the velocity to vary as predicted theoretically (using the linear least squares, curve-fitted velocity).

^eLine source (observed wave amplitude and range only) at the predicted source height listed in method d.

^fLine source (observed period, amplitude, and range): isothermal atmosphere.

^gIterative line source blast wave radius (kinetic energy density conservation): $R_{\text{o}} = 10\text{--}30 \text{ m}$, nominal acoustic efficiency (hypersonic flow modeling).

^hAlthough consistent energetically, this height regime is inconsistent with our acoustic time delay solutions, as noted earlier.

is $\cong 153.3 \text{ s}$ from a source height of 40 km for propagation through a multilayered nonisothermal atmosphere, or $\cong 205.0 \text{ s}$ for a source height of 60 km, for example (for details, see Fig. 8e). In addition, our predicted wave normal “ray”-tracing travel time estimates are also nicely bounded by our above travel time estimates from 154.8 s (based upon the observed trace velocity) to 210.8 s (based on the relative time delay from the time of peak heating). In addition, the Wendover airport is not located at sea level, but at a

geopotential height, $z \cong 1.92 \text{ km}$. This value must be subtracted from the above height estimates when comparisons are made using the wave kinetic energy density conservation approach, for example, since those source height estimates are reckoned upward from the ground ($z = 0$). However, in practice, this only accounts for a systematic decreased travel time of $\sim 4.1 \text{ s}$. In addition to this altitude correction relative to sea level, we have also corrected the array coordinates for the magnetic declination

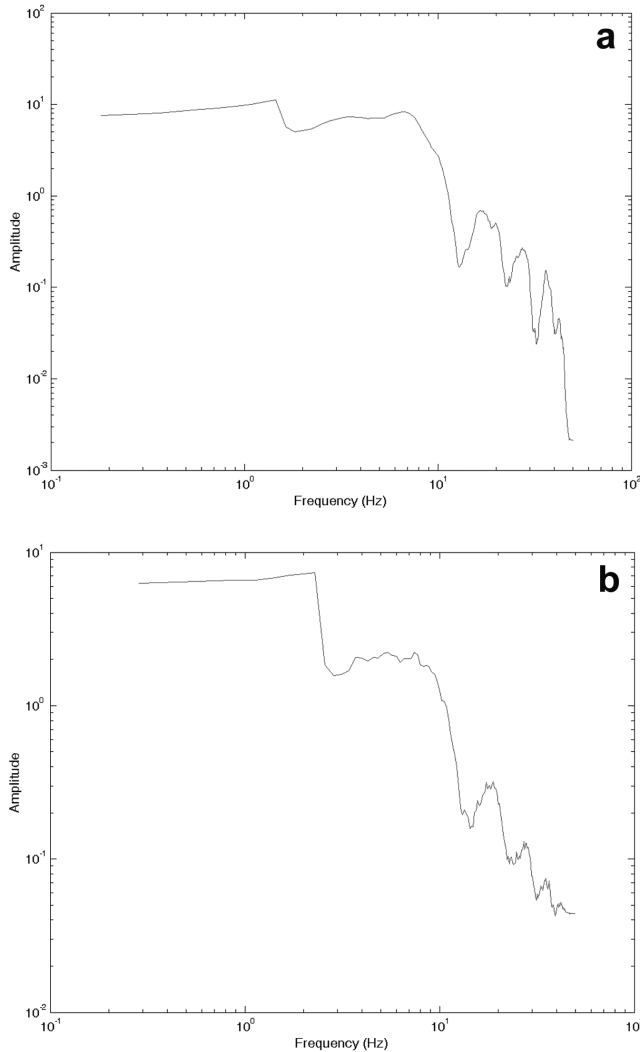


Fig. 6. a) An FFT power spectrum of the initial hypersonic boom arrivals. b) An FFT power spectrum of the second set of arrivals.

deviation of $\approx 15^\circ$ at Wendover. This nontrivial correction resulted in a final plane wave back azimuth using MATSEIS/Infratool (and also using f-k [frequency-wavenumber] analysis) for the initial N wave arrivals of $\sim 200.23^\circ$.

When the Infratool data-processing results indicated in Figs. 10a and 10b were physically interpreted below, we have further determined that the initial arrivals emanated from an intersection point on the trajectory about 43 ± 2 km above sea level, based on the mean ray angle back to the entry trajectory measured from the Wendover infrasound array. A summary of the infrasound detections in Infratool can be made as follows (in terms of the predicted, plane wave back-azimuth variations; see Figs. 10a and 10b for further details):

1. Initial arrival: initially about 200.23° , switching over a short time after the initial arrivals to $170\text{--}180^\circ$ intermittently (we also saw such rapid azimuth variations from infrasound data collected in the western USA at

five LANL infrasound arrays operated during the Space Shuttle Columbia disaster as discussed in ReVelle et al. 2003). Eventually, the back azimuth switches briefly all the way to the north (0°), when a possible reflection off a local mountain range to the north of Wendover apparently occurred.

2. A rapid return to about $205\text{--}210^\circ$.
3. A much more gradual increase of the back azimuth from 210° up to 270° and then with a gradual turning back toward $\sim 250^\circ$ (over an interval of ~ 1 min).

Finally, as is shown in Figs. 11a and 11b, by using the standard seismic MATSEIS f-k location method, we have also independently determined a back azimuth of 200.56° for the initial main hypersonic boom signals that arrived at our Wendover infrasound array as well as a value of 208.11° for the subsequent delayed signals that arrived ~ 10 s later. For the former back azimuths, the intersection point along the entry trajectory close to 43 ± 2 km, referenced to the height of Wendover above sea level, is in reasonable agreement with the Infratool approach (for further details, see Fig. 2).

ACOUSTIC ENERGY AND RAY-TRACING: WAVE NORMAL ARRIVALS

Atmospheric Structure Parameters

In order to ray-trace the wave normal field, we needed the best possible atmospheric temperature (or equivalently sound speed and mean molecular weight) and horizontal wind speed structure available for January 15, 2006. This we determined by utilizing conventional U.S. Weather Service radiosonde ascent balloon data from the station at Salt Lake City and from the data output of MSIS (Hedin et al. 1996) and from the United Kingdom Meteorological Office (UKMO) forecast model. The UKMO winds were found to be superior to the HWM (for predicting the arrival time delay compared with observations). The HWM is the horizontal wind model maintained at the U.S. Naval Research Laboratory in Washington, D.C. (see, e.g., Picone et al. 2002), as will be discussed again later. As discussed below, it was somewhat unusual on this night because the main stratospheric wind field was quite strong and easterly, i.e., from the east and not the normally anticipated westerly winter wind field. These atmospheric structure parameters (mean values of the temperature and horizontal winds) are plotted in Figs. 9a–c below, as indicated earlier.

Top-Down Bottom-Up Ray-Tracing Validity Checks: Wave Normal Path Reconstructions

The results of standard wave normal wave normal ray-tracing in Cartesian coordinates from a supersonic or even a hypersonic source (ReVelle et al. 2004; ReVelle 2005) such as Stardust is provided in Figs. 8a–d. At an entry angle of 8.2° , we are certainly pushing the range of validity of the

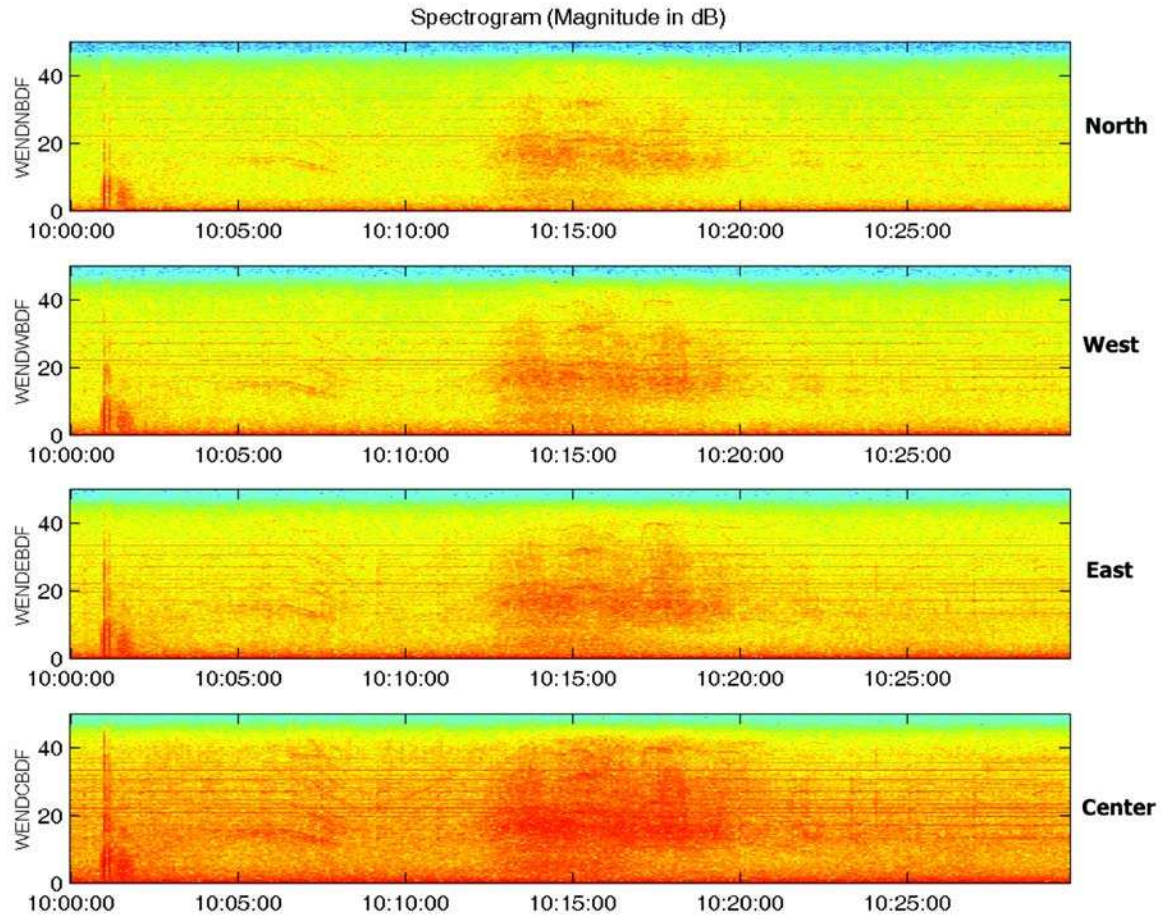


Fig. 7. A spectrogram.

Cartesian coordinate system approach, but it has nevertheless been found useful previously when it was also successfully applied to the Columbia shuttle re-entry disaster of February 1, 2003 (ReVelle et al. 2003).

This approach is similar to the “wave normal” approach that was developed by Hayes et al. (1969), but we have assumed a priori an infinite speed line source so that the complete phase reconstruction of the signals for a rapidly moving point source was not necessary (which is in reality a superior description of the Stardust re-entry acoustic source function). Here we will compare these downward ray-tracing results to those determined previously using Infratool, hence we are doing a top-down bottom-up validity check of our ray-tracing solutions.

We can choose from any of three readily available options to evaluate the characteristic velocity of the acoustical waves as they propagate (one of two kinematic propagation constants of the motion for a perfectly stratified atmosphere), namely:

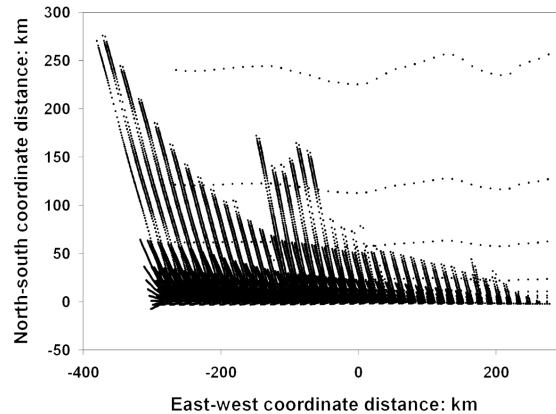
1. Ideal line source (infinite speed source, for an assumed instantaneous energy release).
2. Modified line source (as above, but with blast wave radii corrections for fragmentation).

3. Supersonic, rapidly moving point source with an explicit Mach cone half angle based on a constant speed with respect to the local adiabatic thermodynamic sound speed.

For the Stardust re-entry, option 3 is the most appropriate given the very low entry speed compared with most normal meteor entries; it has been used throughout in Figs. 8a–e.

We have run a number of typical cases for the Stardust re-entry, only the last few of which we will report on here. The nominal set of Stardust entry parameters utilized are as follows: horizontal entry angle (mean) = 8.2° , mean entry speed = 10 km/s (which has a Mach cone half angle with respect to an isothermal, hydrostatic atmosphere = 1.81° , for a mean thermodynamic sound speed = 0.316 km/s) for a mean vector heading of 90.50° (from Dugway Utah, UTTR radar data). For this vector heading, the perpendicular ray toward Wendover, in the absence of horizontal winds, would have an azimuth launch angle toward $\sim 0.50^\circ$. If the finite Mach cone angle is also included in the prediction, the resulting vector heading launch angle is increased slightly, for a straight line path, to $\sim 2.31^\circ$. Our line source wave normal ray-tracing results using (3) are given in Figs. 8a–d. Results in Fig. 8a were computed assuming a 10 km/s mean

- a** Stardust Entry- Line source wave normal paths: Top view in the $\{x,y\}$ plane
 Mean capsule velocity = 10 km/s; Mean horizontal entry angle = 8.2 deg
 Wave normals launched every 2 km from 80 km to the ground ($z = 0$)
 27 normals launched at each height for azimuths up to 60 deg out of the entry plane



- b** Stardust Entry- Line source wave normal paths: Top view in the $\{x,y\}$ plane
 Mean capsule velocity = 3 km/s; Mean horizontal entry angle = 8.2 deg
 Wave normals launched every 4 km from 80 km to the ground ($z = 0$)
 27 normals launched for azimuths up to 60 deg out of the entry plane

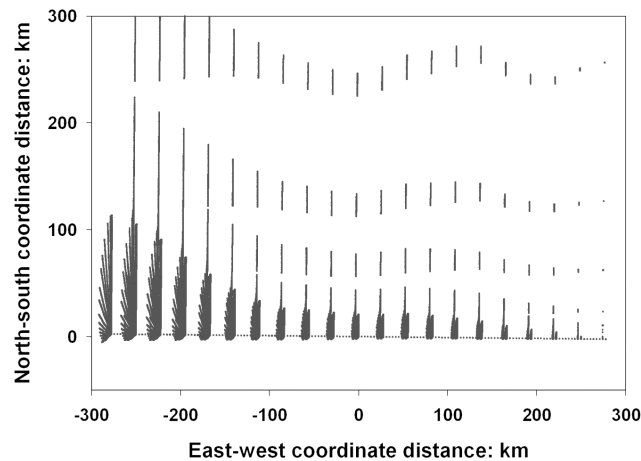


Fig. 8. a) Top view: wave normal analyses for a line source, mean velocity = 10 km/s. Wave normals are launched every 2 km at 27 intervals about the entry plane ($\Delta\phi \cong 0 \pm 60^\circ$) for source heights from 80 km to the ground. b) Top view: wave normal analyses for a line source, mean velocity = 3 km/s. Wave normals are launched every 4 km at 27 intervals about the entry plane ($\Delta\phi \cong 0 \pm 60^\circ$) for source heights from 80 km to the ground.

velocity and results in Fig. 8b assumed a 3 km/s mean velocity over the entire entry trajectory for comparison (this set of parameters was used since the velocity of Stardust at the position of closest approach to Wendover was predicted from our earlier results to be ~ 3 km/s).

The predicted ground arrival angles for our array position at Wendover with respect to Stardust, including the Mach cone half angle effect for a 3.0 km/s mean source speed evaluated for a source altitude of 40 km and a mean sound speed $\cong 0.30$ km/s, are:

1. Azimuth angle: from 180.0° ; vector heading angle = 0.0°
2. Elevation angle = 42.7° ; signal trace velocity = 0.41 km/s
3. Propagation time delay = 2.40 – 4.41 min (see Fig. 8e)

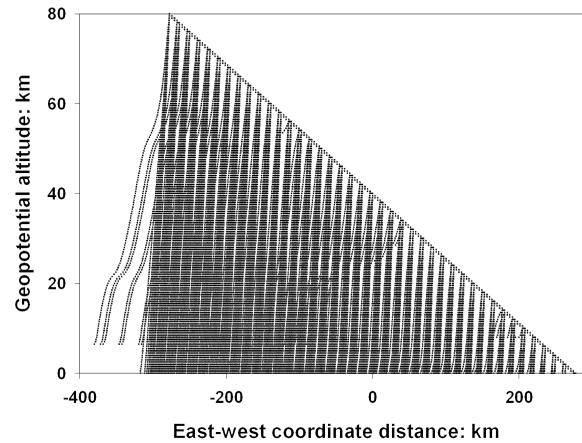
These values can be compared with those generated

during the signal detection and analysis results from Matseis/Infratool, etc., which for plane waves can be summarized as:

- a. Back azimuth: from 200.23° ; vector heading angle = 20.23°
- b. Elevation angle = 50.54° ; signal trace velocity = 0.535 km/s
- c. Propagation time delay = 2.58 – 3.51 min

The latter time delay values in (c) are not actually from Matseis/Infratool itself, but instead are based on travel-time estimates based on external timing constraints provided by NASA. The other values are the results after the correction from geomagnetic north to geographic north was also made (due to a geomagnetic-geographic offset of $\sim 15^\circ$ at the Wendover airport, as noted earlier) and generally agreeing

- c** Stardust Entry- Line source wave normal paths: Sideview looking from the South
 Mean capsule velocity = 10 km/s; Mean horizontal entry angle = 8.2 deg
 Wave normals launched every 2 km from 80 km to the ground (z = 0)
 27 normals launched at each height for azimuths up to 60 deg out of the entry plane



- d** Stardust Entry- Line source wave normal paths: Sideview looking from the East
 Mean capsule velocity = 10 km/s; Mean horizontal entry angle = 8.2 deg
 Wave normals launched every 2 km from 80 km to the ground (z = 0)
 27 normals launched at each height for azimuths up to 60 deg out of the entry plane

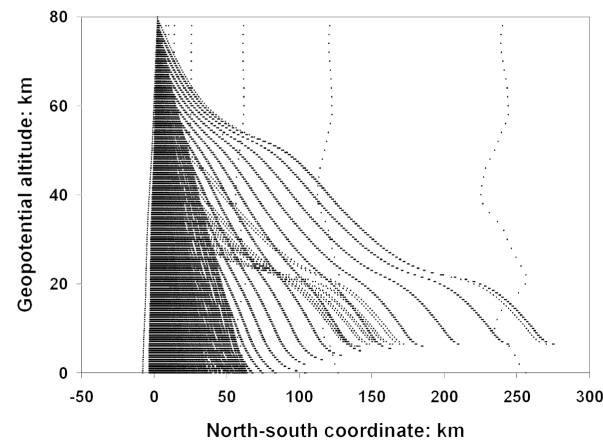


Fig. 8. *Continued.* c) Side view, viewed from the south: wave normal analyses for a line source. Wave normals are launched every 2 km at 27 intervals about the entry plane ($\Delta\phi \cong 0 \pm 60^\circ$) for source heights from 80 km to the ground. (Note: Wendover, Nevada, is located at ~ 1.92 km above sea level.) d) Side view, viewed from the east: wave normal analyses for a line source. Wave normals are launched every 2 km at 27 intervals about the entry plane ($\Delta\phi \cong 0 \pm 60^\circ$) for source heights from 80 km to the ground.

with the ray-tracing results. Thus, we have found agreement between these various methods with the plane wave back azimuth within 20.2° , agreement of the trace velocity within 0.125 km/s (23.1%), and agreement with the elevation arrival angle of 7.8° (15.0%).

Most of the very large discrepancy of the plane wave back azimuth between the two approaches was certainly due to the strong winds aloft during the night of January 15th. In addition, a strong surface and upper-air cold front passed the observing site during a time interval just a few hours before our infrasonic and seismic measurements were made. With such strong frontal winds, it is usual to have large temporally and spatially varying turbulent wind gusts and associated directional changes, and so forth, that are largely unknown

and very hard to quantify. However, the most unusual prevailing meteorological condition was the complete directional reversal of the winds in the stratosphere during this period such that the prevailing winds aloft were easterly and not westerly. In addition, we have also used a constant mean vector heading of the Stardust capsule during entry that may not have been the case at the lower heights near the time of landing as well.

In addition, however, all of the above calculations that were done were generated for a line source path and have assumed a single constant velocity during the entry trajectory, which is also clearly not the case. The complete moving point source problem with significant deceleration is much harder to solve exactly, however, since the correct phase alignment

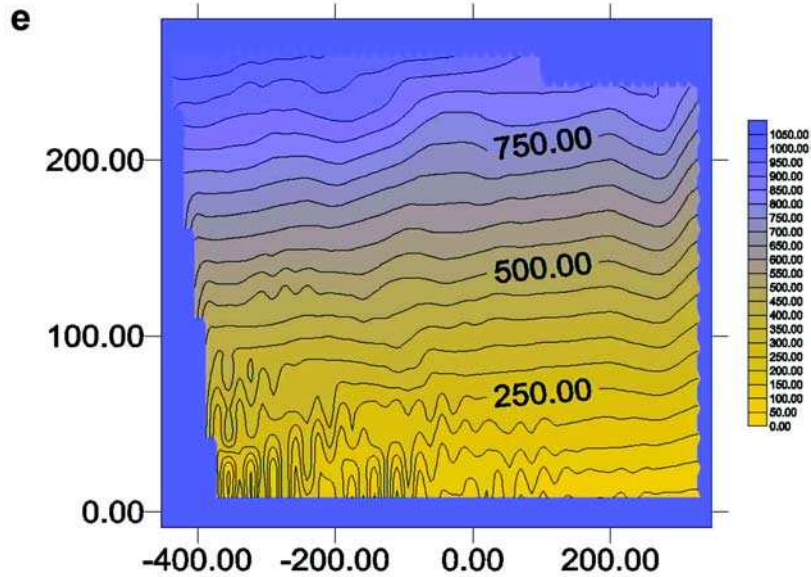


Fig. 8. *Continued.* e) Overhead view in the $\{x,y\}$ plane of the contours of the acoustic travel time (s) to the first bounce condition and beyond (for the nominal Stardust hypersonic boom corridor using the environmental parameters plotted earlier): done every 2 km for 27 wave normals launched at up to $\pm 60^\circ$ from the entry plane for source heights from 80 (left) to the ground (right lower corner).

between various segments of the entry trajectory would also have to be superimposed properly, and so forth. Given the large overall degree of uncertainty in the mean value of the various environmental parameters, we were still satisfied with our results using all of the quite different techniques.

Differential Acoustic Efficiency Evaluations Assuming Wave Kinetic Energy Density Conservation (Inviscid Treatment)

The recently developed method used below is described in detail in ReVelle et al. (2004) and therefore will not be fully described here (for further application details, see also ReVelle 2005). The method is an approach that conserves the wave kinetic energy density (assuming an inviscid medium at these low frequencies at relatively low heights) by iterating the blast wave radius as a free variable (not using the linear, least squares curve fitted blast wave radius in Equations 3a and 4a below) until a match between the differential acoustic efficiency at the source and at the ground observation point are within a specified tolerance (we assumed a matching tolerance = 0.010%). This assumes a direct wave arrival whose total range from the source can be adequately represented as the square root of the sum of the squares of the horizontal range and of the assumed source altitude as a function of the possible plane wave arrival azimuths (see below for further details). Both range dependencies and air density dependencies are explicitly accounted for in this iterative process for either weakly nonlinear or strictly linear acoustic wave propagation whose effects are also explicitly allowed within the iterative numerical algorithm. This procedure has now been fully tested to account for effects in a

non-isothermal atmospheric density and sound speed structure, and so forth (which closely reproduces the U.S. Standard Atmosphere [1976] in either the summer or winter months at middle latitudes).

In contrast to our earlier kinetic energy density conservation results, where range and height were combined to compute a total slant range only along the observed back azimuth direction, we have now included range and height at all possible back azimuths as part of the overall solution with full details given below.

Since the entry angle was known for both entries and quite shallow, we were able to constrain possible values of slant range along different individual azimuths as a function of the altitude of the origin of the acoustical signals. Indicated below, r_\perp is the point of closest approach at the ground to the Stardust and Genesis entry trajectories, respectively, from our infrasound array location in a right-handed orthogonal three-dimensional Cartesian space, $\{x, y, z\}$ with x pointed toward the \perp point of closest approach along the trajectory from the observer.

Thus, we also have the generalized expression:

$$r_{\text{slant}} = \{r_\perp^2 + z^2 + (\Delta y)^2\}^{1/2}; \text{ where } \Delta y = \Delta z / \tan\langle\theta\rangle; \quad (1a)$$

$$\Delta z = z - z_{\text{nom}}$$

where $r_\perp = 26.1$ km for Genesis, $\langle\theta\rangle = 8.0^\circ$; $z_{\text{nom}} = 43.07$ km for Genesis (at the point of closest approach); $r_\perp = 32.6$ km for Stardust, $\langle\theta\rangle = 8.2^\circ$; and $z_{\text{nom}} = 42.7$ km for Genesis (at the point of closest approach).

Each of these solutions can also be distinguished on the basis of the observed back azimuth toward the source with the nominal back azimuth for Genesis $\cong 220.2^\circ$ and for Stardust

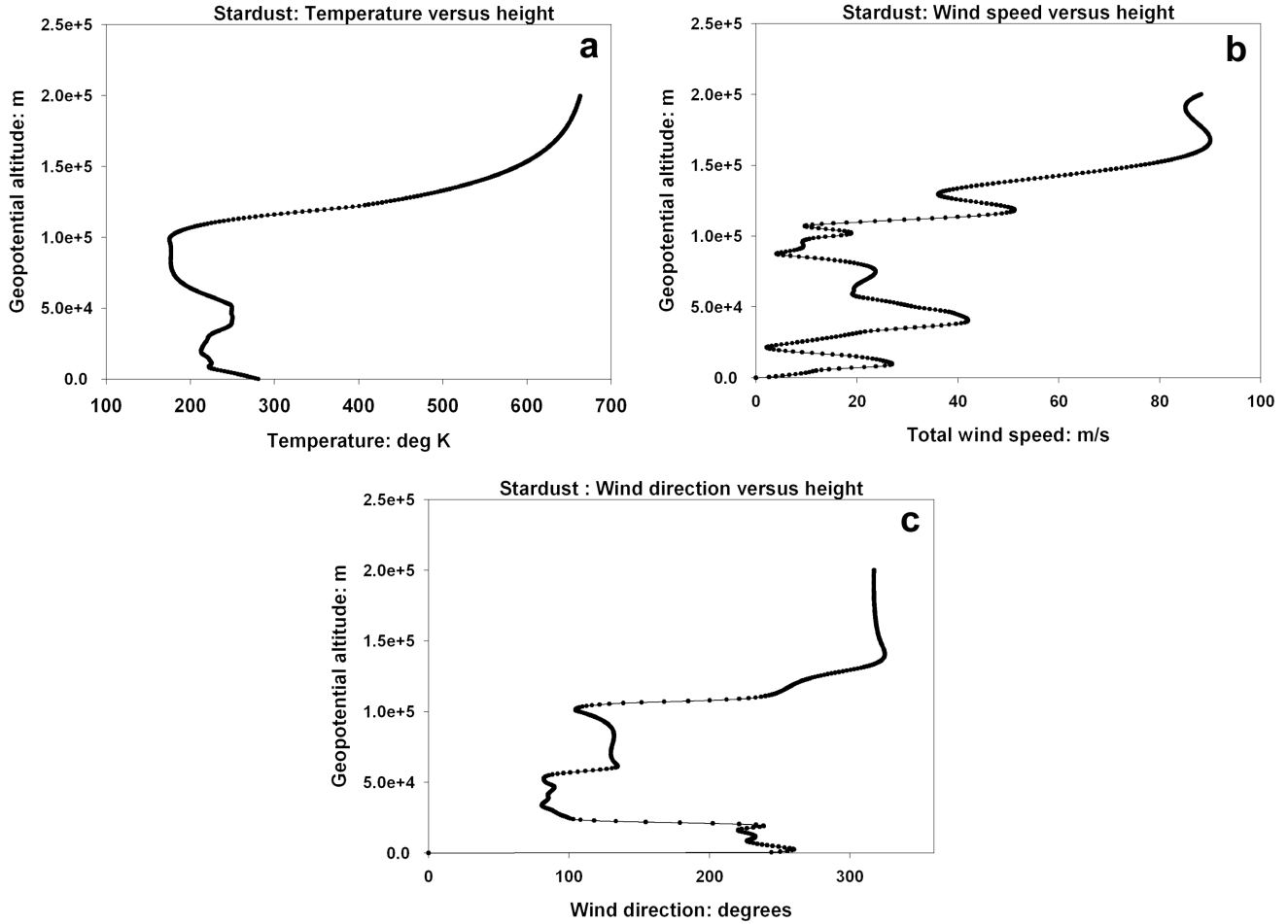


Fig. 9. a) Atmospheric temperature structure versus height in m using radiosonde data (0600Z, September 8, 2004) from Salt Lake City at the lowest heights and using the MSIS-E model aloft. b) Atmospheric total horizontal wind speed structure available from the UKMO model versus height in m . c) Atmospheric horizontal wind direction structure available from the UKMO model versus height in m .

$\cong 200.2^\circ$ for the perpendicular distances given above at the point of closest approach to our infrasonic array. For displacements Δy away from the nominal point of closest approach, we can readily calculate the angular deviation from the nominal back azimuth using:

$$\Delta\alpha \text{ (in degrees)} = (180.0/\pi) \cdot \left\{ \frac{\Delta y/r_{\text{horiz}}}{\{r_{\perp}^2 + (\Delta y)^2\}^{1/2}} \right\}; r_{\text{horiz}} = \quad (1b)$$

For a source height of 60 km, e.g., for Stardust, $\Delta y = 120.05$ km, $r_{\text{horiz}} = 124.4$ km, and the azimuth deviation (from the nominal back azimuth of 210°) = 55.3° , whereas for a source height = 43 km, $\Delta y = 2.082$ km, $r_{\text{horiz}} = 52.64$ km, and the azimuth deviation (from the nominal back azimuth of 210°) = 2.27° .

Revised Equations for Infrasonic Source Energy Analysis

Since we have used the hemispherical shape approximation throughout this paper, Equations 3a and 4 of ReVelle et al. (2004) also need to be appropriately updated.

These energy relations, adapted for the more general case as a function of a constant, mean shape factor, S_f , can now be written in the form (and used in Tables 3a–c solutions for kinetic energy density conservation and used for the source height determinations):

$$E_s(J) = \{ \pi^{3/2} \cdot (1/16.0) \cdot (1.0/S_f^{3/2}) \} \cdot \rho_m \cdot (c_s^7/V) \cdot (\tau/1.579)^4 \cdot (1/R) \quad (2a)$$

$$E_s(J) = \{ \pi^{3/2} \cdot (1/16.0) \cdot (1.0/S_f^{3/2}) \cdot (1.0/k_1^4) \} \cdot \rho_m (c_s^3/V) \cdot R^3 \cdot (\Delta p/p^*)^4 \quad (2b)$$

where $S_f \equiv A/V_0^{2/3} \equiv$ shape factor, A = frontal cross-sectional area, V_0 = meteor volume, k_1 = constant = 0.29164, R = total slant range, ρ_m = meteor bulk density, c_s = adiabatic thermodynamic sound speed, V = meteor velocity, τ = infrasonic wave period, Δp = infrasonic wave amplitude (zero to peak), and p^* = geometric mean pressure (between source and observer).

These are, respectively, the relations in the weak shock propagation regime for the determination of the bolide source

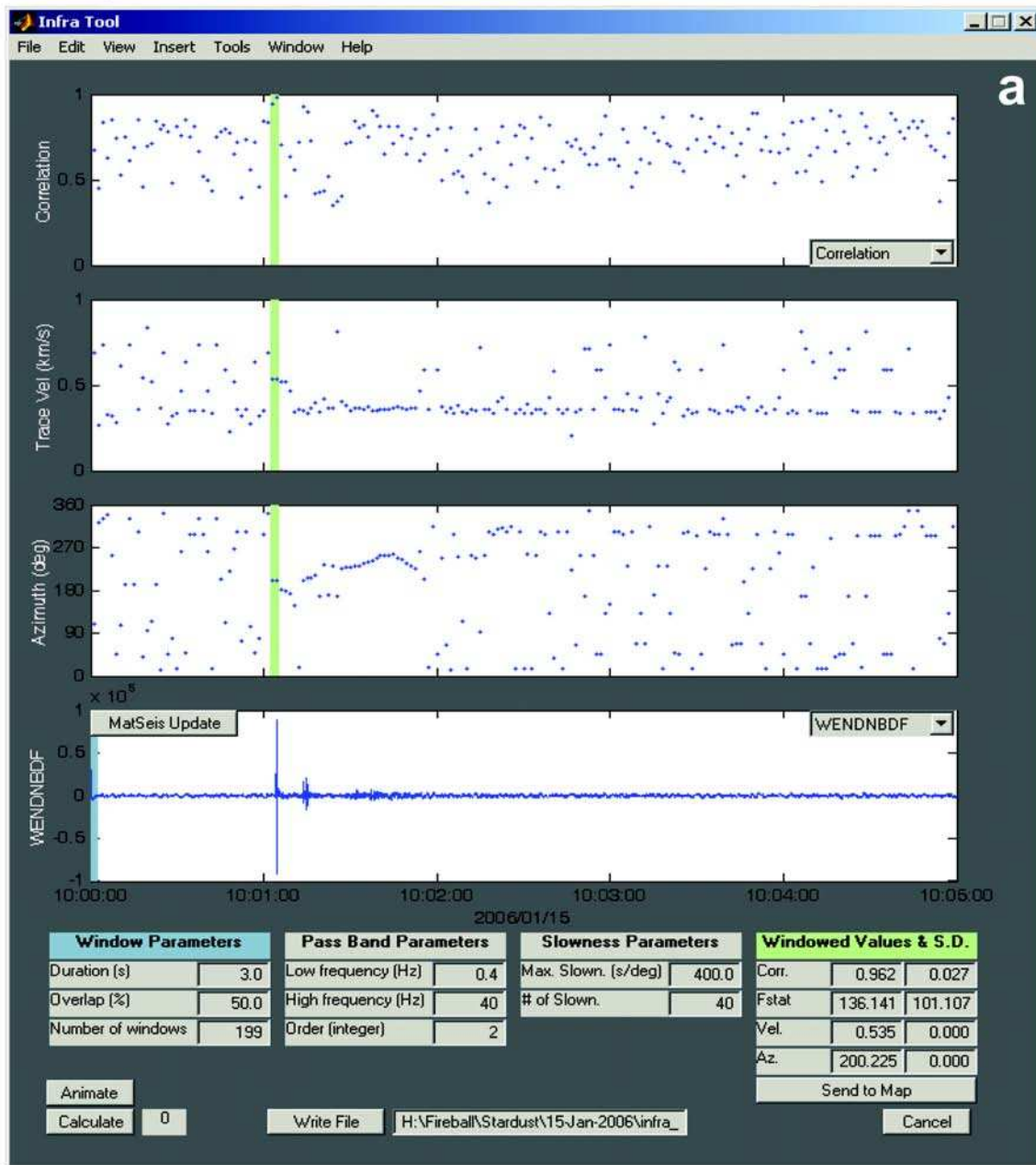


Fig. 10. a) MATSEIS/InfraTool detection: initial N wave arrivals.

kinetic energy in joules assuming a line source blast wave using first only the wave period and range information (Equation 2a) or using wave amplitude and range information only (Equation 2b), respectively. Actually our dynamical/energetic entry solutions utilize the approximation that $\mu = 0.10$ (heavy blunting regime) rather than the simple, self-similar flow regime case where $\mu = 2/3$, which is appropriate if $S_f = \text{constant}$ throughout the entry. The errors involved in the estimation of the source energy by not properly accounting for the detailed variation of the shape factor with height are quite small however in comparison to

all of the other inherent uncertainties and have been neglected here.

Stardust Curve-Fitted Entry Results

After reconstructing the Stardust entry using the approach described earlier, we have determined the following linear, least-squares curve fit parameters over the entire trajectory, all with the geopotential altitude z expressed in km (and derived from the detailed entry dynamics solutions determined above) using the simplest possible exponential form that most naturally describes the entry dynamics solutions:

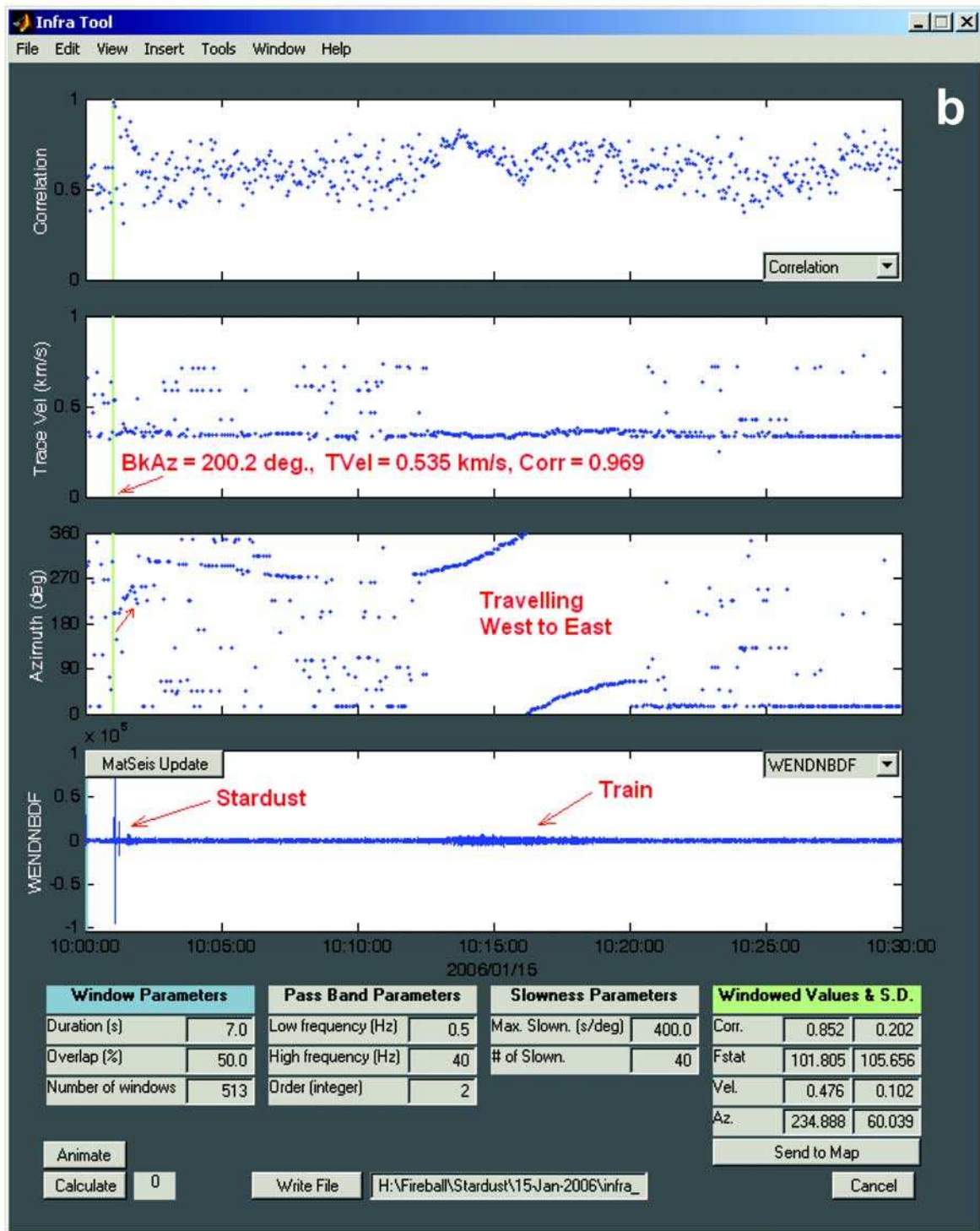


Fig. 10. *Continued.* b) MATSEIS/InfraTool detection: initial N wave and subsequent arrivals.

Blast radius (in m): $r^2 = 0.9992$

$$R_0(z) = y_0 + a \cdot \exp[-bz] \quad (3a)$$

$$y_0 = 44.7237, a = -159.6514, b = 3.477 \cdot 10^{-2}$$

This curve fit solution is not used in the iterative wave kinetic energy conservation algorithm described below, but was used in the computation of the source energy using method (b) in Tables 3a, 3b, and 3c (by matching the predicted wave period compared to the observed wave

period at the ground as a function of horizontal range and height).

Velocity (in km/s): $r^2 = 0.9963$

$$V(z) = y_0 + a \cdot \exp[-bz] \quad (3b)$$

$$y_0 = 13.9250, a = -286.0846, b = 8.114 \cdot 10^{-2}$$

Kinetic energy (in J): $r^2 = 0.9864$

$$KE(z) = y_0 + a \cdot \exp[-bz] \quad (3c)$$

$$y_0 = 6.6289 \cdot 10^9, a = -1.8075 \cdot 10^{10}, \\ b = 2.498 \cdot 10^{-2}$$

Since the appearance of the Genesis re-entry analysis paper, ReVelle et al. (2005), we have uncovered an unfortunate error in the acoustic efficiency calculations that ultimately caused only very poor solutions to be found for the kinetic energy density conservation relations (an incorrect multiplying constant in our FORTRAN computer algorithm for the differential acoustic efficiency was thankfully discovered during the course of the current Stardust investigations). These relations have previously allowed us to find the height of the acoustic waves from the source independently from the time delay of the acoustic waves (ReVelle et al. 2004, 2005). Of course, after correcting the leading constant appropriately, the kinetic energy density conservation equation iterative solution immediately worked properly, as will be shown below. Using the corrected algorithm (as done correctly in ReVelle et al. 2004), the curve fit of the resultant differential acoustic efficiency as a function of height can be expressed in the form:

Differential acoustic efficiency (dimensionless):

$$r^2 = 0.9999$$

$$\varepsilon_a(z) = a \cdot \exp[-bz] \quad (3d)$$

$$a = 171.0080, b = 0.1684; 1/b \sim H_p (\cong 5.938 \text{ km})$$

where H_p = pressure scale height of the equivalent isothermal, hydrostatic atmospheric model.

Kinetic Energy Density Conservation Solutions: We have listed our new numerical solutions in Tables 3a and 3b, first for Stardust and then our revision for the Genesis re-entry in Table 3c, which had the unfortunate numerical error mentioned directly above. We have also plotted these new results for Stardust in Figs. 12a–c. Figure 12a shows our solutions for the nominal set of Stardust values for the initial hypersonic boom arrivals. Figure 12b shows the solution for the second set of infrasonic arrivals for the Stardust re-entry. Although this latter solution is not nearly as good as the one for the initial hypersonic boom arrivals, it is also clear that the source height must be close to that for the initial arrivals. Even on the basis of signal timing alone, this must be the case since there is only <10 s difference in the arrival time of the

second set of arrivals compared to the initial arrivals. This means that for direct air acoustic solutions, the source altitude could not have been very different from the initial arrivals (<~3–4 km). In addition, these delayed signals have much smaller amplitudes and slightly higher frequency content than the initial hypersonic boom arrivals, but their structure and their overall FFT (Figs. 11a and 11b) is very similar to the initial arrivals. The sequence of these latter arrivals discussed earlier may have been in a regime of destructive interference effects (wave defocusing regime), which may account for why linearized hydrodynamic techniques do not seem to work nearly as well as in the “normal” nondefocusing regime. However, an additional and far more probable seismic origin for the proper interpretation of these delayed signals is given in detail in a forthcoming Stardust seismic calibration paper (Edwards et al., Forthcoming).

From results shown in Fig. 12a, it is clear that the source altitude must be ~40 km, as seen earlier using other methods in this paper as well. These graphs directly indicate the regime of the entry dynamics solutions in combination with the kinetic energy density conservation solutions for further clarity. The fact that the two Stardust solutions do not intersect, but are reasonably close to intersecting near 40 km, yet are self-consistent and formally intersect for Genesis is puzzling and will be evaluated further to determine the source of errors involved.

In addition, in order to complete these solutions for both Stardust and Genesis, we have constrained the differential acoustic efficiency values to be $\leq 4\%$, consistent with the fact that uncertainties in the fundamental input values could produce large uncertainties in the final acoustic efficiencies and also consistent with other successful bolide evaluations of these properties (ReVelle et al. 2004). Consistently larger differential acoustic efficiencies would not allow successful solutions for the source heights with all other parameters held constant.

Below the end height for both the Stardust and Genesis re-entries, we have forced a nearly constant slope solution for all four of the entry dynamics variables that were curve-fitted above. This procedure was carried out to ensure continued dynamic continuity of the variables outside of their primary curve-fitted region (calculated down to the panchromatic end height where all entry associated luminosity ceases). This dynamic continuity was especially important for numerical stability during the kinetic energy density wave amplitude calculations, which made use of the kinetic energy and differential acoustic efficiency.

The total power balance for Stardust is plotted in Fig. 4a with the corrected differential acoustic efficiency (see also Fig. 3h for separate acoustic efficiency details for both Genesis and Stardust as a function of height).

It is important to note that although we have utilized a near-replica of the U.S. Standard Atmosphere (1976) in our non-isothermal atmosphere during the kinetic energy

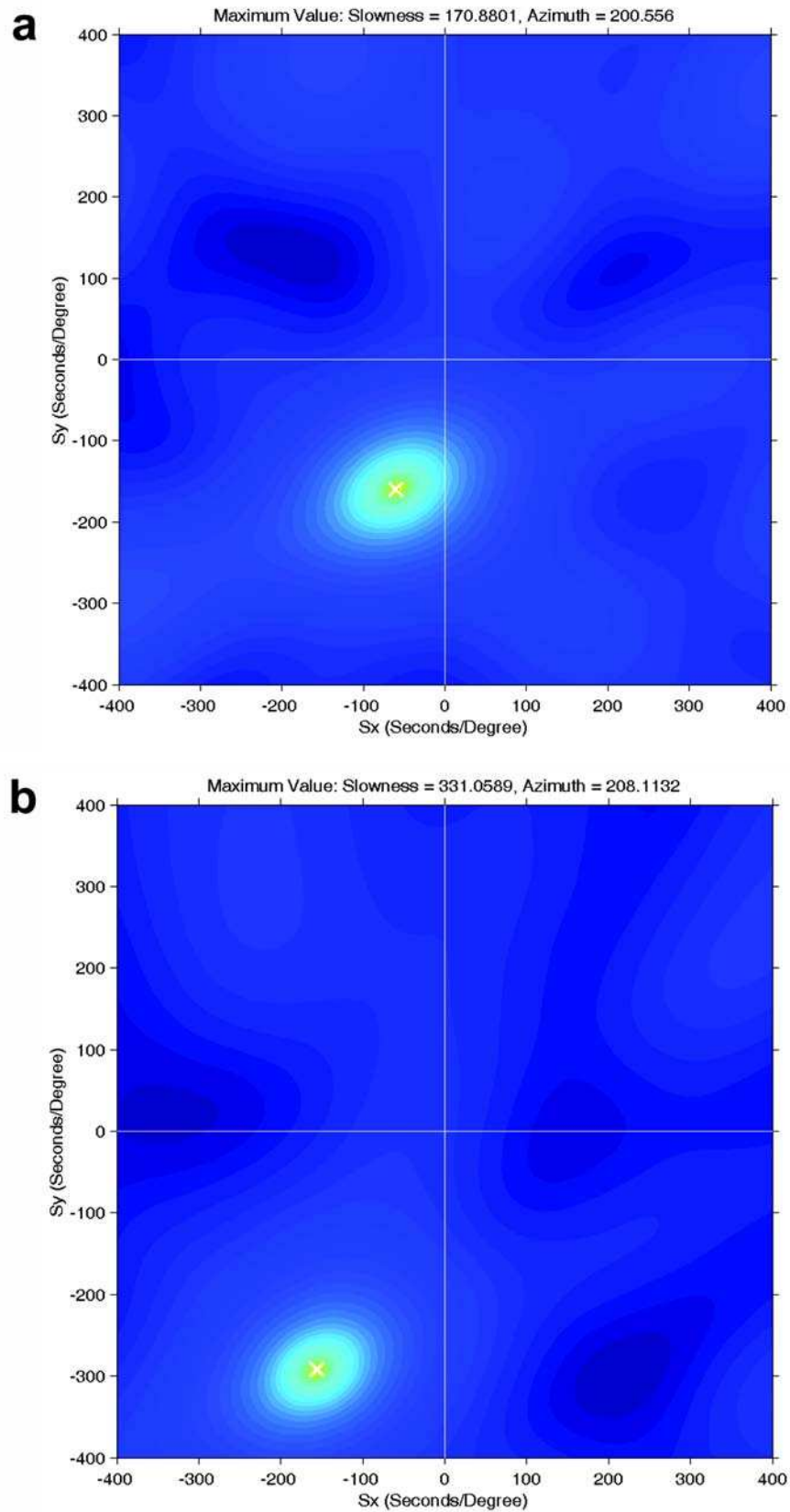


Fig. 11. a) MATSEIS/f-k detection of the initial hypersonic boom arrivals. b) MATSEIS/f-k detection of the second set of delayed arrivals.

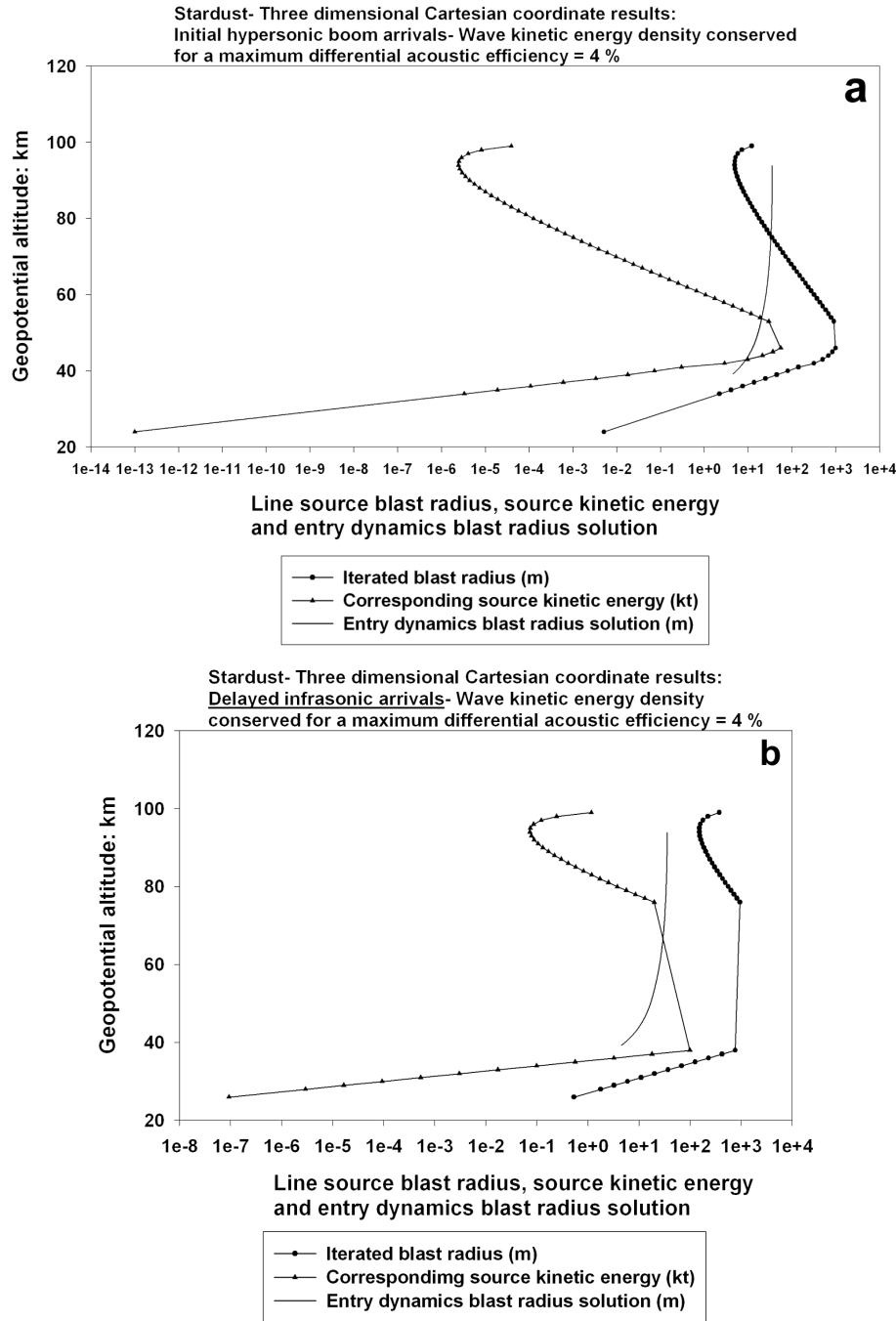


Fig. 12. a) Stardust: kinetic energy density source altitude search with infrasonic data. Initial hypersonic boom arrival with all nominal parameters. b) Stardust: kinetic energy density source altitude search with infrasonic data. Solutions for the second set of arrivals (delayed by about 10 s from the initial arrivals).

density conservations solutions, we have not used precisely the identical atmosphere that was utilized for the wind-speed and sound-speed profiles given earlier for the line-source wave normal, ray-tracing procedures. This difference in the model atmospheres utilized may also account for some for the discrepancies between the predicted altitude results and the observations.

Genesis Curve-Fitted Entry Results (Revised in This Paper)

After reconstructing the Genesis re-entry again using the approach described earlier in this paper, we have determined the following linear, least-squares curve fit parameters over the entire trajectory, all with the geopotential altitude z expressed in km (and derived from the detailed entry dynamics solutions determined

Genesis- Three dimensional Cartesian coordinate results (revised in this paper):
Wave kinetic energy density conserved for a maximum differential acoustic efficiency = 4 %

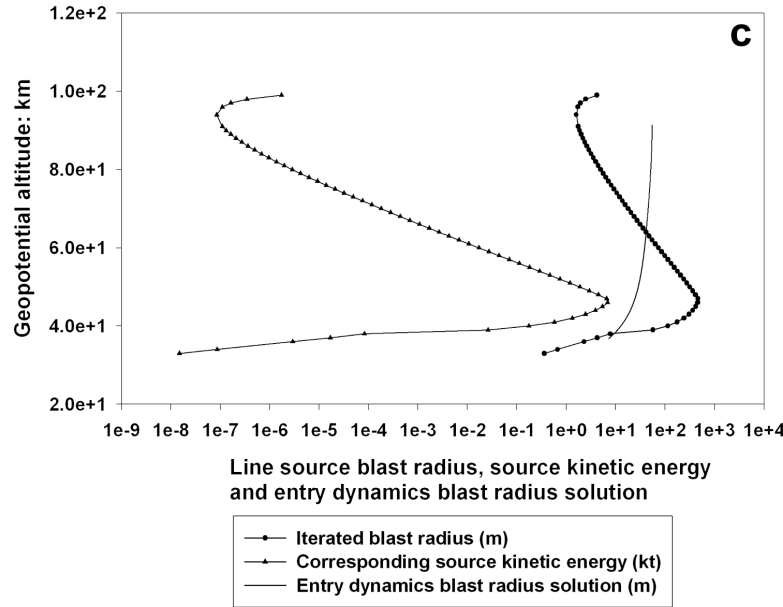


Fig. 12. *Continued.* c) Genesis (revised in this paper): kinetic energy density source altitude search with infrasonic data. Results for the initial hypersonic boom arrival.

above), again expressed in terms of a simple exponential function:

Blast radius (in m): $r^2 = 0.9994$

$$R_o(z) = y_o + a \cdot \exp[-bz] \quad (4a)$$

$$y_o = 60.1293, a = -225.6799, b = 3.91 \cdot 10^{-2}$$

As noted above, this curve fit solution is not used in the iterative wave kinetic energy conservation algorithm, but was used in the computation of the source energy using method (b) in Tables 3a–c (by matching the predicted wave period compared to the observed wave period at the ground as a function of horizontal range and height).

Velocity (in km/s): $r^2 = 0.9967$

$$V(z) = y_o + a \cdot \exp[-bz] \quad (4b)$$

$$y_o = 11.9500, a = -138.5488, b = 7.065 \cdot 10^{-2}$$

Kinetic energy (in J): $r^2 = 0.9869$

$$KE(z) = y_o + a \cdot \exp[-bz] \quad (4c)$$

$$y_o = 2.0497 \cdot 10^{10}, a = -6.5466 \cdot 10^{10},$$

$$b = 3.07 \cdot 10^{-2}$$

Using the corrected algorithm (as in ReVelle et al. 2004), the curve fit of the resultant differential acoustic efficiency as a function of height can be expressed in the form:

$$\text{Differential acoustic efficiency (dimensionless):}$$

$$r^2 = 0.9999$$

$$\varepsilon_a(z) = a \cdot \exp[-bz] \quad (4d)$$

$$a = 51.6909, b = 0.1538, 1/b = H_p (\cong 6.502 \text{ km})$$

where H_p = pressure scale height of the equivalent isothermal, hydrostatic atmospheric model.

Kinetic Energy Density Conservation Solutions: We have listed our new numerical solutions for the Genesis re-entry in Table 3c, which previously had a numerical error as noted above. We have also plotted these new results for Genesis in Fig. 12c, which indicates our solutions for the nominal set of Genesis values only for the initial hypersonic boom arrivals. The Genesis solution in Fig. 12c clearly shows that the Genesis source altitude must also be near 40 km as seen earlier using other methods in this paper as well. This plot also directly indicates the entry dynamics solutions in combination (including their point of intersection as noted earlier above) with the kinetic energy density conservation solutions for further clarity. The revised total power balance for Genesis is shown in Fig. 4b.

Corrected Differential Acoustic Efficiency Results (ReVelle et al. 2005)

Since there have been problems with understanding the behavior of the differential acoustic efficiencies generated at low heights for the lower range of Earth entry velocities, below we will further investigate these effects for nearly spherically shaped, two-dimensional bodies such that $d = L$, where L is the vehicle length and d is its diameter.

Starting from Whitham (1950): far-field result: $R \gg \Lambda$ (R = range; Λ = wavelength):

$$\Delta p_s \cong \{p(z) \cdot p_0\}^{1/2} \cdot \{Ma^2 - 1\}^{1/8} \cdot d^{3/4}/R^{3/4}; \quad (5a)$$

$$Ma = V(z)/c_s(z)$$

where $C_D = f(Ma, Re) \cong 1.0$ in the inviscid aerodynamic drag equation ($= 0.50 \cdot \rho \cdot V^2 \cdot C_D \cdot A$) and as presented in ReVelle et al. (2005).

From ReVelle (1976), for the weak shock wave regime with $Ma \gg 1$ and $Re \gg 1$ (where Re = Reynolds number): $x > \sim 10^2$; $x = R/R_0$ (see below):

$$\Delta p_h \cong k \cdot \{p(z) \cdot p_0\}^{1/2} \cdot \{R_0/R\}^{3/4}; C_D = 0.92, \quad (5b)$$

$$k \cong 0.2917$$

where Re = Reynolds number of the flow, Ma = Mach number, p_0 = surface atmospheric pressure, and $p(z)$ is the atmospheric pressure as a function of altitude.

We have used the value of $C_D \cong 1.0$ for both spheres and cylinders (oriented perpendicular to the axis of the cylinder) for flow Reynolds numbers from $\sim 10^3$ to 10^6 and for Mach numbers from 2 to 12 (White 1974).

We wish to make a transition from using Equation 5b to Equation 5a if $M < M_{crit}$, where M_{crit} is the critical transition Mach number below which supersonic flow field effects are applicable. We will further assume that $M_{crit} \cong 5.0$ so that supersonic flow conditions rather than hypersonic flow conditions prevail during the shock wave generation process at relatively low heights and velocities. Since the wave drag coefficient changes are so small, we will assume the constant value of 0.92 throughout the matching process, even though it is really only strictly applicable to hypersonic large Reynolds number flows. This trade-off between hypersonic and supersonic flow regimes has been done numerically in Mach number steps in our numerical entry modeling code so that changes take place in the values relatively slowly.

Thus, we can write the supersonic flow differential acoustic efficiency corrected for the expectations for supersonic flow, ϵ_{dac} and the hypersonic flow form of the differential acoustic efficiency, ϵ_{dac} in their new respective forms as a function of the shape factor of the body (with R and d canceling completely from the results):

$$\epsilon_{dac} = \{\Delta p_s / \Delta p_h\}^2 \cdot \epsilon_{dac} \quad (5c)$$

$$\Delta p_s / \Delta p_h = [\{Ma(z)^2 - 1\}^{1/8} / \{k \cdot Ma(z)^{3/4}\}] \quad (5d)$$

$$\epsilon_{dac} = k' \cdot \{(4/3) \cdot S_f^{3/2} \cdot \pi^{-1/2}\} \cdot \{p^2(z) \cdot V(z) \cdot l(z) / (\rho(z) \cdot \rho_m R_0(z) \cdot c_s^5(z))\} \quad (5e)$$

Since ϵ_{dac} itself depends upon the pressure wave amplitude squared in the weak shock regime and for a sphere the quantity, $\{(4/3) \cdot S_f^{3/2} \cdot \pi/\pi^{3/2}\} \cong 1.0$.

Performing a units analysis, we also find that the new form of ϵ_{dac} is dimensionless as expected:

$$[\epsilon_{dac}] = \{1/\gamma^2\} \cdot \{\rho(z)/\rho_m\} \cdot \{l(z)/d(z)\} \quad (5f)$$

where $k' = 1.98375 \cdot 10^{-2}$ from first principles, line source blast wave theory at $x = 10$ (where it can be shown that $k \cong 6 \cdot (0.057549)^2$), Δp_s = pressure wave amplitude predicted by supersonic flow theory (Whitham 1950), Δp_h = pressure wave amplitude predicted by hypersonic flow theory (ReVelle 1976), $S_f(z)$ = body shape factor = $A/Vol^{2/3}$, A = frontal cross-sectional area, Vol = meteor volume, $V(z)$ = instantaneous velocity, $l(z)$ = line length, $\rho(z)$ = ambient atmospheric density, ρ_m = bulk density of the body, $R_0(z)$ = line source blast wave relaxation radius without fragmentation ($\cong Ma \cdot d(z)$), $c_s(z)$ = adiabatic thermodynamic sound speed, $x = R/R_0(z)$ = scaled distance compared to the slant range R from the body, $d(z)$ = body diameter

The first result that can be noticed from this new result is that the differential acoustic efficiency for a hemisphere ($S_f \cong 1.9192$) is exactly twice as large as that for a sphere (for which $S_f \cong 1.209$) with all else the same. The other and perhaps less obvious result which comes from manipulations of the above expression is that there is no natural cutoff parameter for the magnitude of ϵ_{dac} where it will start to decrease over time (or over increasingly deeper penetration into the atmosphere) as is the case for the other differential efficiencies shown earlier (see Figs. 4a and 4b for our earlier predictions for Stardust and Genesis, respectively).

Identifying in Equation 5f the key parameters that control the changes in the magnitude of ϵ_{dac} as penetration increases into the atmosphere, we can see that as either $\rho(z)$ increases or $d(z)$ decreases due to ablation at progressively lower altitudes, ϵ_{dac} is predicted to continue to increase. Unfortunately, the only obvious way to get the magnitude of ϵ_{dac} to decrease is through the correction term proposed in Equation 5c from the transition from hypersonic to supersonic flow conditions for Mach numbers $< \sim 5$.

We implemented Equation 5c numerically in our code only if the local Mach number was < 5 . This expression was implemented into our entry code in velocity increments as a function of the transitional Mach number so that large changes did not result as we transitioned from one efficiency form to the other during entry at progressively greater penetration depths. Mach 5 is a clear transition zone for the case of ever increasing speed since above this speed, dissociation of the neutral gas first begins. This is not clearly the case however as speed decreases due to hysteresis in the system as is discussed directly below.

One final comment on the topic of the differential acoustic efficiency for slow objects (natural or man-made) needs to be made. It is not the supersonic phase that has limited the analysis of results, but instead the region where the hypersonic flow approximation transition occurs for the pressure wave amplitude generation process, i.e., where there is no longer an equivalent line source "explosion" taking place. The applicability of the supersonic pressure wave amplitude approximation of Whitham is certainly doubtful above Mach 5, where the hypersonic flow regime is really just

applicable (where dissociation starts as we proceed upward in Mach number from small values to larger values, etc.), but just how low in Mach number we can proceed before hypersonic flow theory is no longer a useful theoretical approximation has not been satisfactorily answered yet. One question that we would like to answer is this: if we were able to reliably specify a limiting Mach number for the hypersonic flow regime, what would the corresponding reduction in the pressure wave amplitude be compared to the full hypersonic “explosion” analogue predictions? Pressure wave amplitude matching is certainly possible between the two sets of results as we have shown above (hypersonic versus supersonic flow theory), but to do this effectively we need to know the transition Mach number where this amplitude matching should be carried out. This uncertainty is partly due to hysteresis in the process so that the range of possible physical effects for increasing Mach numbers is not equivalent to those for a corresponding systematic reduction of the Mach number. Thus, the detailed pressure wave amplitude decay process is not known in enough detail as we progress from large to small Mach numbers as it is as we progress upward from small to large Mach numbers. Finally, the pressure wave generation process that we have now envisioned does not have any natural limiting reduction in the differential acoustic efficiency as deeper penetration into the atmosphere is achieved as noted above, unless either the object actually breaks up while a collective wake fragment behavior occurs as is typical for bolides (for details, see ReVelle 2005) or if the velocity of the nonfragmenting body substantially decreases. All of the other differential efficiencies naturally diminish near the end of the flight as we have now evaluated them (Figs. 4a and 4b). This is not true of the differential acoustic efficiency until a Mach number of about 5 is reached however (if no breaking occurs) where this reduction will naturally occur as the wave amplitude begins to decrease due to a steady reduction in the Mach number of the body at progressively lower heights (as the natural terminal velocity of the body is reached).

Finally, in Fig. 13 we compare the semi-empirical bolide solutions of Edwards et al. (2005) with observations. The semi-empirical bolide model relies on a wind correction factor for the stratospheric wind speed in its predictive capabilities. As noted earlier, two different atmospheric wind models were also used in the analysis for comparison purposes, namely the HWM and the UKMO models. In Fig. 13, we have plotted both the predicted peak-to-peak infrasonic amplitude as a function of the altitude predictions of the two wind models along with the measured value at our array in Wendover at a known range from the entry trajectory. Clearly on this night the UKMO model performs its task far more reliably than does the HWM model for our location in Nevada. Ironically, the predicted winds in the stratosphere were easterly aloft on January 15, which is not a common occurrence. As can be seen, the Edwards et al. approach

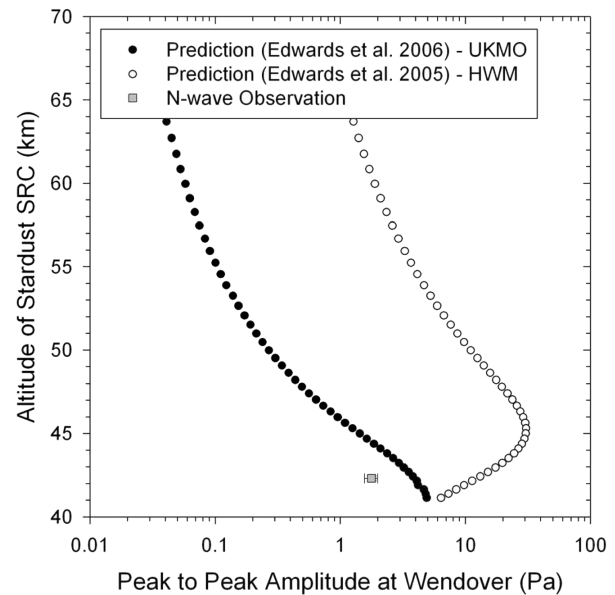


Fig. 13. Semi-empirical bolide solution: solutions for both the HWM and the UKMO wind data. Amplitude as a function of source altitude (km) and peak to peak pressure (Pa) for horizontal range from Wendover, Nevada, from the Genesis entry trajectory.

(2005) demands a source height of ~ 43 km, precisely in a region where our kinetic energy density wave conservation also demands a solution. This deduced height region is also in quite good agreement with the wave normal ray-tracing solutions as well as with the Matseis/Infratool solutions found earlier as well.

SUMMARY AND CONCLUSIONS

Predictions and Measurements

Using an entry model developed by ReVelle (2001, 2002, 2005) and ReVelle et al. (2004, 2005), we have predicted the complete entry dynamics (drag, deceleration, etc.) and associated mass loss (with a concomitant prediction of the ablation parameter and various heat transfer coefficients), the total heating rate as well as the panchromatic luminosity, and so forth, of the entry of Stardust, an artificial, albeit low-velocity “meteor” fall and recovery at UTTR, i.e., at the Dugway Proving Grounds in Utah. The Stardust space capsule re-entered the atmosphere after its seven-year mission in space at about 09:57 UTC (02:57 MST) on January 15, 2006. A four-element infrasound array consisting of pressure sensors was also rapidly deployed at the Wendover, Nevada airport after its transport from Los Alamos. This standard system had a 3 dB band-pass from ~ 0.02 to 300 Hz and the data recorded have been sampled at a rate of 100 Hz. This array allowed us to detect, locate, and categorize the “hypersonic” infrasonic booms from the re-entry of the Stardust spacecraft. We have also used the detailed properties

of the Stardust infrasonic “hypersonic boom” by connecting the various key measurements (wave amplitude, dominant period and range, etc.) back to the blast wave source. This was done using the line source blast wave relaxation radius and the corresponding differential acoustic efficiency parameter that was predicted by relations developed from previous hypersonic entry modeling work for the Genesis re-entry and for large bolides. The differential efficiency was directly predicted as part of our theoretical entry modeling and was least-squares curve-fitted over altitude for inclusion with the wave kinetic energy density conservation predictions for the Stardust hypersonic booms.

We have also independently determined the detailed paths of the wave normals for a hypersonic line source from a local Mach cone consistent with an average speed of Stardust during entry. This has allowed us to connect together our wave signal processing results with results derived from wave normal ray-tracing aloft using a top-down bottom-up approach. We note finally that the predicted maximum panchromatic magnitude for Stardust (again made using the differential luminous efficiency derived from previous bolide modeling calibrations) was about -9 , some three magnitudes less bright than the full moon. Theoretical comparisons made in this paper against an all-sky camera video data taken by the University of Western Ontario, Department of Physics and Astronomy (W. N. Edwards, P. J. McCausland, and P. G. Brown) generally confirm this brightness prediction, although further calibration of the video image is still being pursued at this time.

Future Work

In 2007, the Japanese spacecraft Hayabusa had been predicted to re-enter over Australia, hopefully with a precious cargo of asteroidal material (see also Table 1b) as briefly discussed earlier. This capsule may now be retrievable during re-entry in Australia in 2010, but nonetheless, we continue to routinely and globally monitor large meteor entries using regular data from U.S. DoE/DoD satellites, the numerous ground-based infrasonic arrays of the International Monitoring System, from ground-based reports, and from other sources. These additional bolides should also prove to be very good tests for a further systematic examination of our previously determined bolide relations at low entry velocities more typical of meteorite entry and for meteorite recovery efforts. This is especially the case for the panchromatic semi-empirical luminous efficiency which has been largely calibrated by meteors at much larger entry velocities. This work is also important so that a better understanding of the relative percentage of porous materials in this large bolide mass range can be more adequately quantified. This percentage has numerous implications for the proper calibration of the global meteor influx rate, besides its value in providing a proper taxonomy of available large bolides.

Combining infrasound and satellite data in new and more interesting ways in our theoretical modeling efforts is extremely valuable in helping us to solve the full repertoire of possible behaviors in this most puzzling natural phenomenon.

Acknowledgments—D. O. R. would like to thank Dr. R. W. Whitaker of the Earth and Environmental Science Division at Los Alamos National Laboratory (LANL) for providing the infrasonic equipment and considerable technical assistance for the rapid deployment of the field instrumentation. He would like to acknowledge the support of Dr. John Szymansky and Mr. Mark Hodgson of the LANL, International Space and Response Division (ISR), Research and Development Program Office, and Dr. Herbert Funsten of the ISR Center for Space Science and Exploration Program Office, Dr. Gary Geernaert of the LANL Institute of Geophysics and Planetary Physics Program Office, and finally Mr. Ward Hawkins, Program Manager for the Ground-Based Nuclear Explosion Monitoring Program at Los Alamos for providing the funds needed to perform these measurements and subsequent analyses on relatively short notice. In addition, he would also like to thank Dr. Peter Jenniskens of the NASA SETI Institute, Mountain View, California, for providing additional funds for our travel costs from Los Alamos to Wendover and back. Funds from NASA for this project were supported in part by the NASA Engineering and Safety Center and the NASA Planetary Astronomy Program. We would also like to acknowledge Dr. Prasan Dasai for kindly providing detailed trajectory information as well as velocity data for both the Genesis and Stardust re-entries. Also, discussions prior to the entry with Professor Donald Brownlee of the Department of Astronomy at the University of Washington, the Principal Investigator for the NASA Stardust Mission, proved extremely useful as well.

W. N. E. would like to acknowledge the British Atmospheric Data Centre for allowing him access on the day of the re-entry to the UK Meteorological Office Stratospheric Assimilated Data-Stream. Finally, both authors would like to thank Mr. Philip J. McCausland for his assistance in setting up the temporary infrasound array and the seismic instrumentation and also we would like to express our thanks to Mr. Jim Petersen and the staff at the Wendover, Nevada, airport for kindly allowing use of the observing sites and providing general access to the airfield for the time period of the experiment.

Editorial Handling—Dr. Donald Brownlee

REFERENCES

- Anderson J. D. 2000. *Hypersonic and high temperature gas dynamics*. Reston, Virginia: American Institute of Aeronautics and Astronautics. 690 p.
- Burnett D. 2004. Official NASA Genesis Science Team Meeting

- Report, Mission Status. Jet Propulsion Laboratory, March 14, 2004. 47 p.
- Cates J. E. and Sturtevant B. 2002. Seismic detection of sonic booms. *Journal of the Acoustical Society of America* 111:614–628.
- Edwards W. N., Brown P. G., and ReVelle D. O. 2005. Bolide energy estimates from infrasonic measurements. *Earth, Moon, and Planets* 95:501–512.
- Edwards W. N., Eaton D., McCausland P. J., ReVelle D. O., and Brown P. G. Forthcoming. Calibration of infrasonic to seismic coupling using the stardust sample return capsule shockwave: Implications for seismic observations of meteors. *Journal of Geophysical Research (Solid Earth)*.
- Garrick I. E. and Maglieri D. J. 1968. A summary of results on sonic-boom pressure signature variations associated with atmospheric conditions. NASA Technical Note #D-4588. 27 p.
- Hayes W. D., Haefeli R. C., and Kulsrud H. E. 1969. Sonic boom propagation in a stratified atmosphere, with computer program. NASA Contractor Report #1299. 50 p.
- Hedin A. E., Fleming E. L., Manson A. H., Schmidlin F. J., Avery S. K., Clark R. R., Franke S. J., Fraser G. J., Tsuda T., Vial F., and Vincent R. A. 1996. Empirical wind model for the upper, middle and lower atmosphere. *Journal of Atmospheric and Terrestrial Physics* 58:1421–1447.
- Henderson H. R. and Hilton D. A. 1974a. Sonic-boom ground-pressure measurements from the launch and re-entry of Apollo 16. NASA Technical Note #D-7606. 45 p.
- Henderson H. R. and Hilton D. A. 1974b. Sonic-boom measurements in the focus region during the ascent of Apollo 17. NASA Technical Note #D-7806. 35 p.
- Hilton D. A., Henderson H. R., and McKinney R. 1972. Sonic-boom ground-pressure measurements from Apollo 15. NASA Technical Note #D-6950. 36 p.
- Hubbard H. H., Maglieri D. J., Huckel V., and Hilton D. A. 1964. Ground measurements of sonic-boom pressures for the altitude range of 10,000 to 75,000 feet. NASA Technical Report #R-198. 42 p.
- Jenniskens P., Wercinski P. F., Olejniczak J., Wright M., Raiche G., Kontinos D., Desai P. N., Spalding R. E., Sandquist K., Rossano G., Russell R. W., ReVelle D. O., Hladiuk D., and Hildebrand A. R. 2006. Surface heating from remote sensing of the hypervelocity entry of the NASA Genesis Sample Return Capsule. 44th AIAA Aerospace Sciences Meeting and Exhibit. Reno, Nevada, January 9–12, 2006.
- Jenniskens P., Wercinski P., Olejniczak J., Raiche G., Kontinos D., Allan G., Desai P. N., ReVelle D., Hatton J., Baker R. L., Russell R. W., Taylor M., and Rietmeijer F. 2005. Preparing for the Hyperseed MAC: An observing campaign to monitor the entry of the Genesis sample return capsule. *Earth, Moon, and Planets*, doi:10.1007/s11038-005-9021-2.
- Kanamori H., Mori J., Sturtevant B., Anderson D. L., and Heaton T. 1992. Seismic excitation by space shuttles. *Shock Waves* 2:89–96.
- Picone J. M., Hedin A. E., Drob D. P., and Aikin A. C. 2002. NRLMSISE-00 empirical model of the atmosphere—Statistical comparisons and scientific issues. *Journal of Geophysical Research A* 107:SIA15-1–SIA15-16.
- Plooster M. N. 1968. Shock waves from line sources. NCAR Technical Note #37. Boulder, Colorado: National Center for Atmospheric Research. 84 p.
- Plooster M. N. 1971. Numerical simulations of spark discharges in air. *Physics of Fluids* 14:2111–2123.
- ReVelle D. O. 1976. On meteor-generated infrasound. *Journal of Geophysical Research* 81:1217–1230.
- ReVelle D. O., Mutschlechner J. P., Sandoval T. D., Brown P. G., and Whitaker R. W. 2003. Los Alamos infrasonic signals from the re-entry and break-up of the shuttle Columbia: February 1, 2003. Interim Final LANL Report. 46 p.
- ReVelle D. O., Brown P. G., and Spurný P. 2004. Entry dynamics and acoustics/infrasonic/seismic analysis for the Neuschwanstein meteorite fall. *Meteoritics & Planetary Science* 39:1605–1626.
- ReVelle D. O. 2001. Theoretical Leonid modeling. Proceedings, Meteoroids 2001 Conference. pp. 149–157.
- ReVelle D. O. 2002. Fireball dynamics, energetics, ablation, luminosity and fragmentation modeling. Proceedings, Asteroids, Comets, Meteors Conference 2002. pp. 127–136.
- ReVelle D. O. 2005. Recent advances in bolide entry modeling: A bolide potpourri. *Earth, Moon, and Planets* 95:441–476.
- ReVelle D. O., Edwards W. N., and Sandoval T. D. 2005. Genesis—An artificial, low velocity “meteor” fall and recovery: September 8, 2004. *Meteoritics & Planetary Science* 40:895–916.
- White F. M. 1974. *Viscous fluid flow*. New York: McGraw-Hill. 725 p.
- Whitham G. B. 1950. The behaviour of supersonic flow past a body of revolution far from the axis. *Proceedings of the Royal Society of London A* 201:89–109.
-